The Pennsylvania State University
APPLIED RESEARCH LABORATORY
Post Office Box 30
State College, PA 16804

On Modeling Structural Excitations by Low Speed Turbulent Boundary Layer Flows

by

Y. F. Hwang, W. K. Bonness and S. A. Hambric

Technical Report 03-008
August 2003

Supported by:

Office of Naval Research,
Dr. Kam Ng, Code 333

E. G. Liszka, Director
Applied Research Laboratory

REPORT DOCUMENTATION PAGE

Form Approved
OMB No. 0704-0188

1. REPORT DATE *(DD-MM-YYYY)* 01-08-2003	**2. REPORT TYPE** Technical Report	**3. DATES COVERED** *(From - To)*

4. TITLE AND SUBTITLE
On Modeling Structural Excitations by Low Speed Turbulent Boundary Layer Flows

5a. CONTRACT NUMBER
N00014-00-G-0058

5b. GRANT NUMBER

5c. PROGRAM ELEMENT NUMBER

6. AUTHOR(S)
Y. F. Hwang, W. K. Bonness, and S. A. Habmric

5d. PROJECT NUMBER

5e. TASK NUMBER

5f. WORK UNIT NUMBER

7. PERFORMING ORGANIZATION NAME(S) AND ADDRESS(ES)

Applied Research Laboratory
Post Office Box 30
State College, PA 16804

8. PERFORMING ORGANIZATION REPORT NUMBER

TR 03-008

9. SPONSORING / MONITORING AGENCY NAME(S) AND ADDRESS(ES)
Office of Naval Research
Ballston Tower 1
800 North Quincy Street
Arlington, VA 22217-5660

10. SPONSOR/MONITOR'S ACRONYM(S)
ONR

11. SPONSOR/MONITOR'S REPORT NUMBER(S)

12. DISTRIBUTION / AVAILABILITY STATEMENT

Approved for public release, distribution unlimited

13. SUPPLEMENTARY NOTES

14. ABSTRACT

This report documents the results of an investigation on the modeling of structural excitations by low speed turbulent boundary layer flows. This work critically examines various spectral models, both wavevector-frequency spectra and cross-spectra. Many of these models became available after the publication of the monograph by Blake (1986). These models are used to predict the pressure spectra measured by flush-mounted hydrophones of various size and location on buoyantly propelled vehicles. Predicted hydrophone responses are compared with experimental data. Recent publications by Chase (1991, 1993) and Dowling (1998) demonstrate that near wall viscous shear stress contributions to the low-wavenumber pressures need to be included. By combining the Chase 1987 inviscid flow model with his 1993 semi-empirical shear stress model at low wavenumbers, a so called "Combined Chase Spectrum" is developed and presented as the most comprehensive model for underwater applications. One of the peculiar features of this model is that its pressure spectrum near zero wavenumber is

(continued on next page)

15. SUBJECT TERMS

16. SECURITY CLASSIFICATION OF:			**17. LIMITATION OF ABSTRACT**	**18. NUMBER OF PAGES**	**19a. NAME OF RESPONSIBLE PERSON**
a. REPORT UNCLASSIFIED	**b. ABSTRACT** UNCLASSIFIED	**c. THIS PAGE** UNCLASSIFIED	UU UNCLASSIFIED-UNLIMITED	58	**19b. TELEPHONE NUMBER** *(include area code)*

Standard Form 298 (Rev. 8-98)
Prescribed by ANSI Std. Z39.18

dominated by the viscous shear stresses when $\omega\delta_* / U_\infty < (\approx 10)$ and by the acoustic components when $\omega\delta_* / U_\infty > (\approx 10)$. For the point frequency spectrum, the most recently published model by Smol'yakov (2000) is shown to be the most accurate. Using Smol'yakov's (2000) point frequency model in conjunction with the normalized wavevector-frequency spectrum (normalized by the point frequency spectrum) of either the Modified Corcos or the Combined Chase model, pressure spectra are predicted with reasonable accuracy up to 20 kHz measured by hydrophones from 0.1-inch to 1-inch diameter flush mounted on various buoyancy propelled vehicles. In an analysis using finite-element structural models, cross-spectra are the most convenient form of forcing functions. In this case, the Modified Corcos cross-spectral density function is recommended since no known cross-spectral density function can be obtained to express the inverse Fourier transform of the Combined Chase wavevector-frequency spectrum. The Modified Corcos cross-spectrum is simple and in good agreement with the Combined Chase spectrum in a broad range of subsonic wavenumbers.

TABLE OF CONTENTS

Page Number

LIST OF FIGURES

LIST OF FIGURES (Cont'd)

1.0 INTRODUCTION

For a ground vehicle (in air) and a submerged vehicle (in water), the turbulent boundary layer (TBL) flow on its surface is essentially incompressible flow because the Mach number, *M*, of a ground vehicle is about one-tenth while for a submerged vehicle it's about one-hundredth. The direct aero- or hydro-acoustic radiation from a smooth vehicle body in the equilibrium flow region is believed to be small since the efficiency with which turbulence energy is converted to radiated sound is proportional to the fifth power of Mach number. The near field pressure fluctuations beneath a TBL, the pseudo sound, however, are intense. They feed energy into a structure and result in structural vibrations. The subsonic vibratory energy may subsequently convert into sound due to scattering by structural discontinuities such as rib-stiffeners, joints, frames, and bulkheads, etc. In a shell structure, sound may also radiate directly from the acoustically efficient membrane and shear wave vibrations.

This report is the first of a series of reports to document the result of recent research on modeling the forcing function and predicting the flow-induced vibration and noise from a submerged vehicle body. This work was funded by the Office of Naval Research (ONR Code 333, Dr. Kam, Ng, the Scientific Officer) under the Torpedo Stealth Technology Program (Contract No. N00014-00-0058-17), from FY1999 to FY2001.

Analyses of the vibroacoustic response of a structure to the stochastic loading by TBL pressure fluctuations have been investigated extensively over the past forty years. Classical analyses were focused on the flow-induced vibrations of infinite plates and finite flat panels (Powell, 1958; Davies, 1971; Blake, 1986). The TBL forcing function is commonly expressed as the second moment of statistics of the pressure field, the space-time correlation function, or its Fourier conjugate, the wavevector-frequency spectrum. The partial (temporal) Fourier transform of the space-time correlation function, the cross-spectral density function, is also frequently used. For an infinite plate, analyses were performed in the wavenumber-frequency domain via the spatial-temporal Fourier transforms of both the forcing function and the structural impulse response function. For a finite panel, analytical solutions are usually obtained via the eigenfunction (or modal) expansion method. The modal force auto- and cross-spectra can be calculated either directly from the integration of the triple product of the TBL cross-spectral density function and two eigenfunctions each of which specifies the generalized displacements at two separated points of the panel, or from a wavenumber-frequency analysis using the wavevector-frequency spectrum and the spatial Fourier transform of the eigenfunctions.

A submerged vehicle body is most likely a cylindrical body that includes several segments of rib-stiffened shells, elastic joints, appendages, internal machinery and its support structures. It is difficult for analytical models to account for the details of these complexities. Using Finite-element structural models created by commercial computer software, such as the SARA-2D or 3D code, is more tractable. When finite element models are used, the forced response can be calculated directly from the frequency response function of structures and the TBL cross-spectral density function. With this application in mind, this effort is not only focused on the wavevector-frequency spectra but also on the cross-spectral density function.

A recent comparison of models for the wavenumber-frequency spectrum of turbulent boundary layer pressures was published by Graham (1997). His work focused on the pressure fields of airframes at subsonic flows. A broad general overview and some reflection on forty years of research of the subject were given by Bull (1996). The purpose of this work is, however, to focus on a critical assessment of the various wavevector-frequency spectral models as well as the corresponding cross-spectral density function models for marine structures. A theoretical overview on turbulence-structure interactions and the mechanisms that cause the low-wavenumber spectra are discussed in great detail. A few prospective models have been evaluated with respect to their consistency with theory and data. Eventually, a model is selected that reflects the current state-of-the-art. A limited verification of the model has been provided by comparing the analytical results using the proposed forcing function model with the hydrophone data reported by Haddle and Skudrzyk (1969) and Abarbanel, Katz, and Cembrola (1994) from buoyancy propelled test models. The agreement between the predicted values and measured data are reasonably good.

Due to the rather limited available data, the model is not presented as having been thoroughly validated. However, this model is presented to the marine acoustics community for further validation, or refutation, with the data that may be available to the broader community. In the mean time, the authors will also continue to examine the model with new data obtained in future experiments.

2.0 TURBULENCE-STRUCTURE INTERACTIONS

In the field of vibration and acoustics where a structure is exposed to turbulent boundary layer flows, the common interest is to know the time history or the frequency spectrum of the vibration and noise. Turbulent pressures on the surface of the structure are unrepeatable and are randomly fluctuating signals both in time and space, but structures have rather well behaved spatial and temporal characteristics. In highly subsonic flow, the predominant spatial scales of the wall pressure fluctuations are extremely small and the pressures measured by a finite sensor vary with the size and shape of the sensor. Structural wave scales are usually much larger than the predominant TBL scales. In an infinite homogeneous plate beneath a homogeneous TBL flow, the predominant small scale convective pressures will produce no net force to excite the larger scale plate bending waves. Plate bending wave vibrations can only be excited by the TBL pressure components of the matching scales. These are the so-called low-wavenumber components of the TBL pressures, which are believed two to several orders of magnitude smaller than the predominant higher wavenumber convective components. Understanding the generating mechanisms and quantifying the levels of the low-wavenumber TBL wall pressure components have progressed rather slowly during the past four decades because of measurement complexities and theoretical controversies (Blake, 1986). Structural response may be expressed as a summation of certain modes, which lower order modal length scales are of the order the dimension of the structure. At any instance of time, the distributed fluctuating pressures produce a net force on the structure, which may be expressed as a summation of a number of individual modal forces. At this point, it may be worthwhile to give a brief overview of how the modal forces are determined and handled in the analysis involved with a stochastic force field. The purpose of this discussion is to provide some justification and rational on reaching the recommended model, which is dramatically different from the well known Corcos model (Corcos, 1963).

Based on classic analyses, the governing equations of a homogeneous planar vibrator can be written as follows:

$$m\frac{\partial^2}{\partial t^2}w(\boldsymbol{x},t)+Lw(\boldsymbol{x},t)=p(\boldsymbol{x},t) \tag{1}$$

where m is the mass per unit area, L is a linear stiffness operator, and w and p are the plate displacement and the external force per unit area, respectively. Both w and p are functions of position vector $\boldsymbol{x} = (x_1,x_3)$ and time t. In this report, we use x_1 and x_3 to denote the streamwise and spanwise coordinate, respectively. The solution, $w(\boldsymbol{x},t)$, of this differential equation can be expressed as the following series expansion in eigenfunctions, $\psi_\mu(\boldsymbol{x})$,

$$w(\boldsymbol{x},t)=\sum_\mu a_\mu(t)\psi_\mu(\boldsymbol{x}) \tag{2}$$

where $a_\mu(t)$'s are time dependent constants which are treated as the generalized coordinates in the function space. Eigenfunctions, $\psi_\mu(\boldsymbol{x})$, and the corresponding eigenvalues, ω_μ^2 are the discrete sets of functions and values that satisfy the boundary conditions and

$$\omega_\mu^2 m\psi_\mu(\boldsymbol{x})=L\psi_\mu(\boldsymbol{x}), \tag{3}$$

which is the result of substituting $\psi(\boldsymbol{x},t)=\psi(\boldsymbol{x})\exp(-i\omega t)$ into the homogeneous part of Eq. (1). Substituting Eqs. (2) and (3) into Eq. (1) and multiplying both sides with the factor $\psi_\nu(\boldsymbol{x})$, then integrating all terms over the surface of the plate results in,

$$M_\nu\ddot{a}_\nu(t)+\omega_\nu^2 M_\nu a_\nu(t)=F_\nu(t) \tag{4}$$

and

$$F_\nu(t)=\int_A p(\boldsymbol{x},t)\psi_\nu(\boldsymbol{x})d\boldsymbol{x} \tag{5}$$

where M_ν is the mode mass, $F_\nu(t)$ is a generalized or modal force, and the simplicity of Eq. (4) is due to the orthogonality of eigenfunctions. Once the modal force is determined the modal response to the excitation can be calculated from Eq. (4). It is extremely important to note that the net excitation force as a function of time is the instantaneously area integrated force, as shown by Eq. (5). The following discussion will show the relationship between the modal force and the space-time correlation function.

2.1 Modal Force, Space-time Correlation Function and Wavevector-Frequency Spectrum

If an ensemble average is performed (shown by the upper bars) on the product of modal forces, i.e.,

$$\overline{F_\mu(t)F_\nu(t')} = \overline{\iint_A p(x,t)\psi_\mu(x)dx \cdot \iint_A p(x',t')\psi_\nu(x')dx'}. \qquad (6)$$

Obviously, the left-hand-side is the cross-correlation of the modal forces. In order to obtain this correlation function, one first needs to obtain the area integrated force shown by Eq. (5) at any instance of time and then proceed with the ensemble average. This is what actually happens in the real physical situation. Since $p(x,t)$ is not a deterministic variable, evaluation of Eq. (5) is not possible except when a statistical simulation such as the Monte Carlo method is used. However, after applying the standard procedure in random analysis that deterministic variables such as $\psi_\nu(x)$ are unaffected by statistical averages in Eq. (6), one has

$$\overline{F_\mu(t)F_\nu(t')} = \iint_A \iint_A \psi_\mu(x)\overline{p(x,t)p(x',t')}\psi_\nu(x')dx'dx$$

where $\overline{p(x,t)p(x',t')}$ is by definition the space-time correlation function of the pressure field. Assuming p is a stationary and homogeneous random process, then the modal force cross-correlation is only a function of a temporal shift, i.e., $R_{\mu\nu}(\tau) = \overline{F_\mu(t)F_\nu(t+\tau)}$. Similarly, the space-time correlation function of the pressure is only a function of a spatial shift, ξ, (separation distance between two points) and a temporal shift, τ. That is, $R_p(\xi,\tau) = R_p(x-x',\tau) = \overline{p(x,t)p(x',t')}$. Accordingly,

$$R_{\mu\nu}(\tau) = \iint_A \iint_A \psi_\mu(x)R_p(x-x',\tau)\psi_\nu(x')dx'dx$$

The Fourier transform of the above expression with respect to τ leads to

$$F^2_{\mu\nu}(\omega) = \iint_A \psi_\mu(x) \iint_A \Gamma_p(x-x',\omega)\psi_\nu(x')dx'dx \qquad (7)$$

where $F^2_{\mu\nu}(\omega)$ is the modal force cross-spectral density function which is the Fourier transform of the modal force cross-correlation function, $R_{\mu\nu}(\tau)$; and $\Gamma_p(\xi,\omega)$ is the cross-spectral density function of the pressure field which is the partial Fourier transform (with respect to τ only) of the space-time correlation function, $R_p(\xi,\tau)$.

The wavevector-frequency spectrum is the spatial and temporal Fourier transforms of the space-time correlation function and is accordingly the spatial Fourier transform of the cross-spectral density function, i.e.,

$$\Phi_p(k,\omega) = \frac{1}{(2\pi)^2}\int_{-\infty}^{\infty}\int_{-\infty}^{\infty}\Gamma_p(\xi,\omega)\; e^{-ik\cdot\xi}d\xi_1 d\xi_3. \qquad (8)$$

The modal force cross-spectrum can also be evaluated in the wavevector-frequency domain if one defines the Fourier transform of the eigenfunction in such a way that

$$S_\nu(\boldsymbol{k}) = \int_{-\infty}^{\infty}\int_{-\infty}^{\infty} \psi_\nu(\boldsymbol{x}) e^{i\boldsymbol{k}\cdot\boldsymbol{x}} dx_1 dx_3 \qquad (9)$$

where the value of $\psi_\nu(\boldsymbol{x})$ must vanish outside the area of the structure. The integration limits in Eq. (7) can then be extended from $-\infty$ to ∞, and it is obviously equal to the integral of the product of $\psi_\mu(\boldsymbol{x})$ and the convolution, $\int_{-\infty}^{\infty}\int_{-\infty}^{\infty} \Gamma_p(\boldsymbol{x}-\boldsymbol{x}',\omega)\psi_\nu(\boldsymbol{x}')d\boldsymbol{x}'$. The Fourier transform of the convolution is $\Phi_p(\boldsymbol{k},\omega)\, S_\nu(\boldsymbol{k})$. Based on Parseval's theorem on the integral of the product of two functions, the integral shown by Eq. (7) can be equivalently evaluated by

$$F_{\mu\nu}^2(\omega) = \int_{-\infty}^{\infty}\int_{-\infty}^{\infty} S_\mu^*(\boldsymbol{k})\Phi_p(\boldsymbol{k},\omega)S_\nu(\boldsymbol{k})d\boldsymbol{k}\,. \qquad (10)$$

The modal force auto-spectrum is then obviously,

$$F_{\nu\nu}^2(\omega) = \int_{-\infty}^{\infty}\int_{-\infty}^{\infty} \Phi_p(\boldsymbol{k},\omega)\left|S_\nu(\boldsymbol{k})\right|^2 d\boldsymbol{k}\,, \qquad (11)$$

which is the wavenumber sum of the product of two power spectra, the wavevector-frequency spectrum of the pressure field and wavevector spectrum of the mode.

The space-time correlation function is a real value function which may be considered as a 3-D extension of the auto-correlation function in the time series analysis. In an ergodic process, an ensemble average may be substituted by a more tractable sample average. For example, in a random sample of time series, the auto-correlation function can be obtained as follows: A given sample function of time is multiplied by the same function shifted by a given time interval (τ); the average value of this product over a sufficient extent of time constitutes one point of the auto-correlation function of a particular shift. A complete auto-correlation function can then be obtained by repeating the process for all values of the time sift. Similarly, if one can obtain a random sample in space and time, $p(x_1, x_3, t)$, the space-time correlation function at a spatial and temporal shift, (ξ_1, ξ_3, τ), can be obtained by the following averaging over a sufficient extend in both space and time, i.e.,

$$R(\xi_1,\xi_3,\tau) = \frac{1}{T}\int_{-T/2}^{T/2}\frac{1}{A}\iint_A p(x_1,x_3,t)\; p(x_1+\xi_1,x_3+\xi_3,t+\tau)dx_1dx_3dt;\quad T,A\to\infty \qquad (12)$$

When this process is repeated for all necessary values of (ξ_1, ξ_3, τ), the space-time correlation function can be displayed by plotting it as a function of (ξ_1, ξ_3, τ). The data in the original record, $p(x_1, x_3, t)$, which is usually lengthy in time and space, can now be compressed into a much shorter function of (ξ_1, ξ_3, τ). This averaging process has caused the loss of detailed spatial and temporal signatures of the random sample, i.e., one can no longer recover the original record using the space-time correlation function. The original phase information is also lost. Like an auto-correlation function corresponds to a power spectrum in frequency, a space-time correlation function, shown in Eq. (12), corresponds to a power spectrum in wavenumber and frequency. The space-time correlation function defined above can therefore be used to determine the modal force auto- and cross-spectra of an elastic structure.

The spatial averaging shown above is essential since the net excitation force as a function of time is the instantaneously area integrated force [see Eqs. (5) and (6)]. This point may be further exemplified as follows. Let $P(k_1,k_3,\omega)$, $P(k_1',k_3',\omega')$ and $\Phi_p(k_1,k_3,\omega)$ be the Fourier transforms of $p(x_1,x_3,t)$, $p(x_1',x_3',t')$ and $R(\xi_1,\xi_3,\tau)$, respectively. The right-hand-side of Eq. (12) is the convolution between $p(x_1,x_3,t)$ and $p(x_1',x_3',t')$ of negative shifts. The Fourier transform of the convolution, Eq. (12) is therefore,

$$\Phi_p(k_1,k_3,\omega)=\frac{P(k_1,k_3,\omega)P^*(k_1,k_3,\omega)}{AT}, \quad (A,T)\rightarrow\infty$$

or the Fourier transform of the pressures, $P(k_1,k_3,\omega)$ and $P(k_1',k_3',\omega')$, must be orthogonal, i.e.,

$$\Phi_p(k_1,k_3,\omega)\ \delta(k_1+k_1')\delta(k_3+k_3')\delta(\omega+\omega')=\overline{P(k_1,k_3,\omega)P(k_1',k_3',\omega')}\ ,$$

which means $P(k_1,k_3,\omega)$ must be orthogonal with respect to ensemble average. This can be guaranteed only when both the spatial and temporal averaging are carried out in a sample average.

We have discussed at this point the relationship between the modal force spectrum of a planar structure and the space-time correlation function (or its Fourier conjugate, the wavevector-frequency spectrum). The choice to use the space-time correlation function or the wavevector-frequency spectrum in analysis may depend on personal preference or on what kinds of analyses are involved. For example; when one needs to evaluate the TBL induced noise on an imbedded sonar array (Blake, 1986), it would be most convenient to conduct analysis in the wavevector-frequency domain. However, it will be more convenient to use the space-time correlation function or the cross-spectral density function to compute the flow-induced vibration of a structure when a numerical model, such as a finite-element model, is used to represent the structure (Hwang, 1998; Hambric and Hwang, 2000).

2.2 Two-Point Correlation and the Corcos Cross-Spectrum

In order to determine the space-time correlation function discussed above, the time histories of a 2-D array of a large number of small pressure sensors must be recorded. This is not practically feasible. The time averaged two-point cross-correlation function had consequently been velocity fluctuations in turbulent flows. The main purpose of this measurement was to understand the structure of turbulent flows such as the effective convection velocities and the average life-times of eddies of various sizes. The two-point velocity correlation peaks for pairs of values of ξ (streamwise separation) and τ (time delay) are such that $\xi/\tau=U_c$ is approximately constant and equal to the local mean velocity. This velocity is called the convection velocity. Early measurements by Willmarth (1958) revealed that the pressure field at the wall reflected similar behavior. Obtaining the space-time correlation function without carrying out spatial averaging may be justifiable based on the Taylor hypothesis that space correlation and temporal correlation are simply related through the convection velocity. It may also be argued that space average can be substituted as a time average in an ergodic process. Generally speaking, the two point pressure cross-correlation is obtained by time averaging over a sufficient amount of time the product of the time history recorded at a point (x_1,x_3,t) and that recoded at a different point with a time shift, $(x_1+\xi_1,x_3+\xi_3,t+\tau)$:

$$R(\xi_1,\xi_3,\tau)=\frac{1}{T}\int_{-T/2}^{T/2}p(x_1,x_3,t)p(x_1+\xi_1,x_3+\xi_3,t+\tau)dt;\quad T\rightarrow\infty. \qquad (13)$$

When the above correlation is measured with zero spatial shift, one obtains the autocorrelation function, of which the Fourier transform yields the frequency spectrum.

The cross-spectral density function, $\Gamma(\xi_1,\xi_3,\omega)$, may be obtained by the Fourier transform of $R(\xi_1,\xi_3,\tau)$ with respect to τ. It may also be determined from the filtered narrow band cross-correlation. Corcos [1963, 1964] used the data from narrow band cross-correlation measurements to come up with the well-known Corcos cross-spectral density function. Corcos [1964] argued that since $R(\xi_1,\xi_3,\tau)$ is a real function, its Fourier transform with respect to time,

$$\Gamma(\xi_1,\xi_3,\omega)=(1/2\pi)\int_{-\infty}^{\infty}R(\xi_1,\xi_3,\tau)e^{-i\omega\tau}d\tau,$$

must have a real part symmetric in ω and an imaginary part anti-symmetric in ω. For the streamwise correlation (at zero lateral shift) in particular, the correlation function and the cross-spectrum must be related by:

$$\begin{aligned} R(\xi_1,0,\tau) &= \int_{-\infty}^{\infty}\Gamma(\xi_1,0,\omega)e^{i\omega\tau}d\omega \\ &= \int_0^{\infty}\left|\Gamma(\xi_1,0,\omega)\right|\cos(\omega\tau+\alpha)d\omega \end{aligned} \qquad (14)$$

If the output of two pressure sensors separated by (ξ, 0) is filtered by two identical narrow band filters of unit width, the averaged (over time) value of the product of their output $R_\omega(\xi,0,\tau)$ is a non-decaying periodic function of τ, i.e.,

$$R_\omega(\xi,0,\tau)=\left|\Gamma(\xi,0,\omega)\right|\cos(\omega\tau+\alpha).$$

The amplitude and phase angle, α, of $\Gamma(\xi,0,\omega)$ are therefore readily measured. Since $\xi/\tau=Uc$, the phase angle and the average translation velocity are related by $\alpha= -\omega\xi/Uc$. In practice, the narrow band space correlations are often measured with zero time delay, τ=0. In this case, the phase angle is simply determined by $\alpha=\tan^{-1}[\mathrm{Im}\,\Gamma(\xi,0,\omega)/\mathrm{Re}\,\Gamma(\xi,0,\omega)]$ (Farabee and Casarella, 1991). Accordingly, when the trivial imaginary term is included, Eq. (14) becomes,

$$R(\xi_1,0,\tau)=\int_{-\infty}^{\infty}\left\{\left|\Gamma(\xi_1,0,\omega)\right|e^{i\omega\xi/U_c}\right\}e^{i\omega\tau}d\omega. \qquad (15)$$

The term inside the bracket, { }, represents the cross-spectral density function. The ratio between the amplitude of the unit bandwidth cross-correlation, $\left|\Gamma(\xi_1,0,\omega)\right|$ and the square root of the product of auto-spectra at (x_1, 0) and ($x_1+\xi$, 0) is the narrow band cross-correlation coefficient,

$$A=\left|\Gamma(\xi_1,0,\omega)\right|/\sqrt{\phi_p(x_1,\omega)\,\phi_p(x_1+\xi,\omega)}\,.$$

In a homogeneous field, $\phi_p(x_1,\omega)=\phi_p(x_1+\xi,\omega)=\phi_p(\omega)$ and A is defined by

$$A=\left|\Gamma(\xi_1,0,\omega)\right|/\phi_p(\omega)\,.$$

Based on the data available at the time (Willmarth and Wooldridge, 1962; Corcos, 1962), Corcos found that A is approximately a function of $\omega\xi/U_c$ only, while U_c/U_∞ is a weak function of $\omega\delta^*/U_\infty$ and ξ/δ^*. Both the magnitude and the argument of $\Gamma(\xi_1,0,\omega)$ are therefore a function of the similar variable $\omega\xi/U_c$, which indicates that the narrow band temporal and space correlation are similarly related through the convection velocity. From Eqs. (14) and (15), the streamwise cross-spectral density function is now obviously,

$$\Gamma(\xi_1,0,\omega)=\phi_p(\omega)A(\omega\xi_1/U_c)\,e^{i\omega\xi_1/U_c}\,. \qquad (16)$$

Based on the lateral correlation measurements by Willmarth and Wooldridge (1962) and Bakewell, et al. (1962), the data suggested the lateral cross-spectrum to be

$$\Gamma(0,\xi_3,\omega)=\phi_p(\omega)B(\omega\xi_3/U_c)\,, \qquad (17)$$

and according to Eq. (15),

$$R(0,\xi_3,\tau=0)=\int_{-\infty}^{\infty}\phi_p(\omega)B(\omega\xi_3/U_c)d\omega\,.$$

The lateral cross-spectrum was verified by Corcos (1964), since the comparison between the measured and computed $R(0,\xi_3,\tau=0)$ using the measured values of $\phi_p(\omega)$ and $B(\omega\xi_3/U_c)$ was excellent. Finally, Corcos assumed his well known cross-spectral density function as,

$$\Gamma(\xi_1,\xi_3,\omega)=\phi_p(\omega)C(\omega\xi_1/U_c,\omega\xi_3/U_c) \tag{18}$$

where C is a rectangular product of A and B, i.e.,

$$C(\omega\xi_1/U_c,\omega\xi_3/U_c)=A\left(\omega\xi_1/U_c\right)B\left(\omega\xi_3/U_c\right)e^{i\omega\xi_1/U_c}.$$

In highly subsonic flow, the predominant spatial scales of the wall pressure fluctuations are small and the pressures measured by a finite sensor vary with the size and shape of the sensor. The attenuation of wall pressure by a finite size pressure transducer causes the uncertainty of spatial resolution of the pressure field. The uncertainty of spatial resolution also causes the uncertainty of pressure resolution in time. This motivated Corcos (1963, 1967) to investigate quantitatively the attenuation of TBL wall pressure frequency spectral density as well as the cross-spectral density by a finite pressure sensor. In order to accomplish this, he needed a specific analytical model of the TBL pressure cross-spectral density function. Based on a careful inspection of data obtained in fully developed pipe flow experiments available at the time, Corcos (1963) proposed to express the above general forms of the correlation functions more specifically as

$$A\left(\omega\xi_1/U_c\right)=\exp\left(-\alpha_1\left|\omega\xi_1/U_c\right|\right), \tag{19}$$

and

$$B\left(\omega\xi_3/U_c\right)=\exp\left(-\alpha_3\left|\omega\xi_3/U_c\right|\right), \tag{20}$$

where α_1 and α_3 are the longitudinal and lateral decay rates of the coherences, whose typical range of values are 0.10-0.12 and 0.7-1.2, respectively.

2.3 Corcos' Wavevector-Frequency Spectrum

The Corcos' wall pressure wavevector-frequency spectrum can be obtained by taking the spatial Fourier transform of Eq. (18), i.e.,

$$\Phi_p(\boldsymbol{k},\omega)=\frac{1}{(2\pi)^2}\int_{-\infty}^{\infty}\int_{-\infty}^{\infty}\Gamma(\boldsymbol{\xi},\omega)e^{-i\boldsymbol{k}\cdot\boldsymbol{\xi}}d\xi_1 d\xi_3 \tag{21}$$

which results in

$$\Phi_p(\boldsymbol{k},\omega)=\phi_p(\omega)\ \left(U_c/\omega\right)^2 f_{corcos}(\tilde{k}_1,\tilde{k}_3) \tag{22}$$

and

$$f_{corcos}(\tilde{k}_1,\tilde{k}_3)=\left\{\frac{\alpha_1}{\pi\left[\alpha_1^2+(1-\tilde{k}_1)^2\right]}\right\}\left\{\frac{\alpha_3}{\pi\left[\alpha_3^2+(\tilde{k}_3)^2\right]}\right\} \tag{23}$$

where the wavevector, $\boldsymbol{k}=(k_1,k_3)$, is the Fourier conjugate of $\boldsymbol{\xi}=(\xi_1,\xi_3)$, and $\tilde{k}_1 = k_1U_c/\omega$ and $\tilde{k}_3 = k_3U_c/\omega$ are the similarity wavenumbers or the normalized streamwise and spanwise wavenumbers, respectively. The wavevector-frequency spectrum is now expressed as $\phi_p(\omega)(U_c/\omega)^2 f(\tilde{k}_1,\tilde{k}_3)$ where $f(\tilde{k}_1,\tilde{k}_3)$ is a normalized dimensionless wavevector spectrum, i.e., $f(\tilde{k}_1,\tilde{k}_3)=\Phi_p(k_1,k_3,\omega)/[\phi_p(\omega)(U_c/\omega)^2]$, which is the Fourier transform of the correlation function, $A(\omega\xi_1/U_c)B(\omega\xi_3/U_c)\exp\left(i\omega\xi_1/U_c\right)$, and according to Eq. (22), the integrated sum of $f(\tilde{k}_1,\tilde{k}_3)$ over wavevector plane, $(\tilde{k}_1,\tilde{k}_3)=(U_c/\omega)^2(k_1,k_3)$, should be unity. Therefore, $f(\tilde{k}_1,\tilde{k}_3)$ indicates merely how the narrow band frequency density is distributed over the wavevector plane.

The low wavenumber components have been identified as the main source of the TBL excitation of a large structure because the high wavenumber components are averaged out on the structural surface in a way similar to the attenuation of the TBL wall pressures by a finite sensor. For a large clamped plate, the structural acceptance of TBL excitation is contributed mainly in a narrow wavenumber band centered on the plate flexural wavenumber which is, in most practical situations, much lower than the convective wavenumber. There is no clear cut definition of the low-wavenumber region; this region covers the subconvective wavenumber range usually within the range where $-0.25 < k_1/k_c < 0.25$, and where, $k_c = U_c/\omega$, is the convective wavenumber. As shown in Fig. 1, the Corcos' wavevector-frequency spectrum is predominantly convective and the low-wavenumber contents are extremely low; they are not observable when plotted in linear scales. When the spectrum is plotted in a logarithmic scale, however, the low-wavenumber region of the spectrum is now graphically observable and varying slowly (wavenumber white) in the region.

Since $\alpha_1^2 \ll 1$, Corcos's $\Phi_p(\boldsymbol{k},\omega)$ at zero and convective wavenumbers, is then approximately,

$$\Phi_p(\boldsymbol{k},\omega)\approx\phi_p(\omega)\left(\frac{U_c}{\omega}\right)^2\begin{cases}\alpha_1/\pi^2\alpha_3, & (k_1,k_3)\to(0,0)\\ 1/\pi^2\alpha_1\alpha_3, & (k_1,k_3)\to(k_c,0)\end{cases}. \tag{24}$$

The effects of convection and the decay of turbulence on the wavenumber-frequency spectrum (Keith and Abraham, 1997) is then obvious. The zero wavenumber spectrum is approximately α_1^2 (≈ 0.01) times that at the convective ridge and therefore it is about 20 dB lower than the convective ridge level. However, this low-wavenumber level is believed to be about 20 dB higher than experimental values. The supersonic region of the spectrum ($|k|/k_c \ll 1$) is a small region within the low-wavenumber region and could be the source of sound radiation contributed by the fluctuating dipoles according to Curle (1955). The high level low-wavenumber white spectrum discussed above may indicate a significant sound radiation from a very low speed turbulent boundary layer flow over a rigid surface even though the flow is virtually incompressible. However, many well known theories indicate the contrary. For example, Kraichnan (1955), Phillips (1955) and Chase (1980, 1987) have shown that the low-wavenumber pressure spectrum of an incompressible turbulent flow must vanish at zero wavenumber; i.e., $\Phi_p(\boldsymbol{k},\omega) \rightarrow 0$ as $k_i \rightarrow 0$. This theoretical result also has a severe implication: an incompressible turbulent boundary layer flow over an infinitely large smooth rigid plate will exert no net normal fluctuating force on that plate.

The Corcos cross-spectral density function shown by Eqs, (18-20) was fitted with measured data within the range, $0.7\omega\delta^*/U_c < \omega\xi_1/U_c < 10$. There is no data available for $\xi_1 < 0.7\delta^*$ and $\xi_1 > 10U_c/\omega$. The analysis conducted by Corcos for the evaluation of the finite size transducer attenuation involved double area integrals of the product of the cross-spectral density function and the two transducer response kernels over the transducer surface. Each response kernel relates the area-averaged output of the transducer caused by a unit pressure at a given point of the transducer. Using the above cross spectral density functions was satisfactory for a small sensor. For a large sensor such as a rigid piston, the evaluation of the integrals must be carried out over large values of $\boldsymbol{\xi}=(\xi_1,\xi_3)$. In this case, Corcos pointed out that using Eqs. (18-20) is not fully justifiable and potentially inaccurate, because the coherence for such large spatial separation is not known. For example, for a circular piston of 1 meter diameter, the required information about the correlation must be valid for ξ_1 as large as 1 meter. The data available for ξ_1, however, are less than 0.16 meter ($=10U_c/\omega$) at 1000 Hz when U_c=10 m/s. In addition there is also a lack of correlation information when the longitudinal separation is small, say $\xi_1 < 0.7\delta^*$.

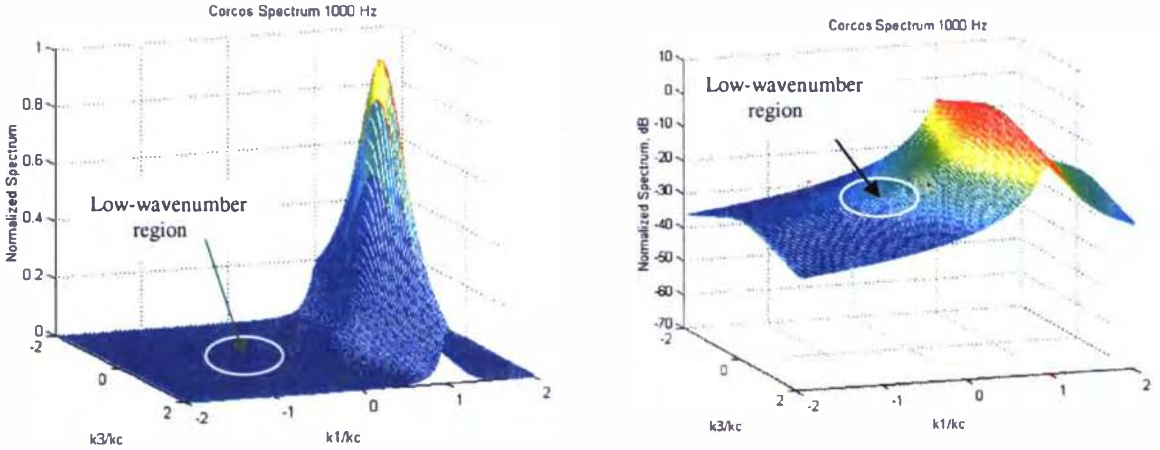

(linear-linear plot) (linear-log plot)

Figure 1. Corcos's Normalized Wavevector Spectrum Plotted in Linear and Logarithmic Scales

Since obtaining the wavevector-frequency spectrum via a spatial Fourier transform involves integrations over large values of $\boldsymbol{\xi}=(\xi_1,\xi_3)$, using the cross-spectral density function shown in Eqs. (18-20) is again not appropriate. Corcos (1964) also indicated that the magnitude of

$\Gamma(\xi_1, 0, \omega)$ is a measure of the convective memory of a frequency component of the wall pressure. Therefore, Corcos's cross-spectrum is dominated by the convective pressure components and, as pointed out by Chase (1980), its corresponding wavevector–frequency spectrum is only valid at and near the convective wavenumber. Since a direct measurement of the space-time correlation function as indicated by Eq. (12) is not feasible, the crucial low-wavenumber spectrum must be measured experimentally. The wavevector-frequency spectrum may then be empirically fitted with data. From this one may also find the space-time correlation function and the cross-spectrum by inverse Fourier transform of the wavevector-frequency spectrum.

2.4 Kraichnan-Phillips Theorem and Chase's Wavevector-Frequency Spectra

Seven years before Corcos' model was published, Kraichnan (1956) investigated the pressure fluctuations exerted on a flat plate by incompressible turbulent boundary layer flows. In underwater applications, the flow is incompressible due to the very small Mach number. Kraichnan (1956) rewrote the incompressible Navier-Strokes equation that led to the Poisson equation for pressure fluctuation, p:

$$\nabla^2 p = -\rho \frac{\partial^2 v_i v_j}{\partial x_i \partial x_j} \tag{25}$$

where v is the particle velocity and ρ is the fluid density. A concise description of the Kraichnan theorem given by Dowling (1998) will be summarized as follows:

For an inviscid flow over a rigid surface S with normal $\boldsymbol{n}$, the pressure must satisfy the boundary condition

$$\boldsymbol{n} \cdot \nabla p = 0 \tag{26}$$

A Green function G(x/y) for Laplace's equation that satisfies the boundary condition can be used to recast Eq. (25) into the integral form:

$$p(x,t) = \int_V G(x/y) \frac{\partial^2}{\partial y_i \partial y_j} \rho v_i v_j (y,t) d^3 y \tag{27}$$

In the case of an infinite plane surface, $y_2=0$, G is just the half space Green function. Accordingly, Eq. (27) can be simplified to

$$\begin{aligned} p(x,t) &= \frac{1}{4\pi} \int_V \left(|x-y|^{-1} + |x-y^*|^{-1} \right) \frac{\partial^2 \rho v_i v_j (y,t)}{\partial y_i \partial y_j} d^3 y \\ &= \frac{1}{2\pi} \int_{V, y_2>0} |x-y|^{-1} \frac{\partial^2 \rho v_i v_j (y,t)}{\partial y_i \partial y_j} d^3 y \end{aligned} \tag{28}$$

where V denotes the half space, $y_2 > 0$, and y^* is the mirror image of the point y with respect to $y_2=0$. Let $P_s(\boldsymbol{k},\omega)$ and $\rho V_{ij}(y_2,\boldsymbol{k},\omega)$ be the Fourier transform (with respect to x_1, x_3, and t) of pressures on the surface, $p_s(x_1,0,x_3,t)$, and Reynolds stress, $\rho v_i v_j(x_1,y_2,x_3,t)$, respectively. The half space Green function becomes one-dimensional, i.e., $G(y_2) = -e^{-|\boldsymbol{k}|y_2}/|\boldsymbol{k}|$ (Ffowcs Williams, 1982; Eq. 2.15). This leads to

$$P_s(\boldsymbol{k},\omega) = \frac{k_i k_j}{|\boldsymbol{k}|}\int \rho V_{ij}(y_2,\boldsymbol{k},\omega)e^{-|\boldsymbol{k}|y_2}dy_2 \qquad (29)$$

where $\boldsymbol{k}$ is the planar wavevector, $\boldsymbol{k}=(k_1,k_3)$. Since the wavevector-frequency spectrum and the pressure Fourier transform are related by

$$\Phi_p(\boldsymbol{k},\omega)\delta(\boldsymbol{k}-\boldsymbol{k}')\delta(\omega-\omega') = \overline{P_s(\boldsymbol{k},\omega)P_s(\boldsymbol{k}',\omega')},$$

Eq. (29) indicates a $|\boldsymbol{k}|^2$ dependency for the wavevector-frequency spectrum known as the Kraichnan-Phillips (1956) theorem for incompressible inviscid flows. A further analysis was carried out by Kraichnan to examine the behavior of $P_s(\boldsymbol{k},\omega)$ at $\boldsymbol{k}=0$. He concluded that the limiting value of $P_s(\boldsymbol{k},\omega)$ as $\boldsymbol{k} \rightarrow 0$ is zero and the integral of the pressure correlation over the boundary surface must vanish.

Also published in 1956, Phillips' work aimed at investigating the strength of an acoustic dipole that could cause aerodynamic surface sound from a plane turbulent boundary layer. He starts with the similar governing equations used by Kraichnan, but instead of solving the differential equations, he performed a stochastic average of the equation and then integrated it with respect to the position variable throughout the space outside the boundary surface. By applying Gauss's theorem and boundary conditions (normal velocity at the surface and the contributions over the surface at infinity vanish), the integrated and stochastically averaged differential equation was reduced to the following important relationship: The surface integrated normal stress is equal to the volume integrated time-derivative of liner momentum. From this, he showed that the mean-square momentum per unit area (the momentum of the fluid in a large area squared, averaged and then divided by the large area) of a shear layer over a flat plate must vanish at low-speed incompressible flow. Consequently, the dipole sound radiated per unit area must also vanish, which means the pressure spectrum must be zero at zero wavenumber. Kraichnan and Philips results were also referred to as Kraichnan-Philips' low-wavenumber constraints by Ffowcs Williams (1982).

Chase (1980, 1987, 1991, 1993) is a seminal contributor of this field. The well known Chase model was first published in 1980. This is perhaps the first descriptive modeling of the wavevector-frequency spectrum for incompressible inviscid flows that follows the Kraichnan-Phillips low wavenumber constraints. His model was developed based on a comprehensive analysis of the fluctuating velocity field statistics and the existing low-wavenumber pressure data available at that time. The low-wavenumber spectrum is thus proportional to the square of the wavenumber and vanishing at zero wavenumber; i.e., $\Phi_p(\boldsymbol{k},\omega) \rightarrow 0$ as $(k_1, k_3) \rightarrow 0$. In the followup paper (Chase, 1987), Chase reexamined the character of the wavevector-frequency spectrum and modified the spectrum to be wavenumber independent (or white) and consistent with experimental data in the subconvective domain, $1/\delta < k_1 << \omega / U_c$, where δ is the boundary layer thickness. For the region, $\omega/c < k_1 < 1/\delta$, the spectrum varies as k^2 to be consistent with Kraichnan-Phillips Theorem. He also extended the spectrum to the acoustic domain with the inclusion of slight fluid compressibility [i.e., Eq. (25) is replaced by the Lighthill's equation] such that acoustic components are generated by the incompressible source terms, the Reynolds stress field. This model has been widely used and was summarized in a recent text book by Howe (1998) with a slight modification.

Unlike the Corcos wavevector-frequency spectrum, the Chase spectrum is not explicitly separable between the frequency spectrum and the wavevector spectrum. By carefully examining the Chase 1987 model according to the form arranged by Howe (1998), the approximated expressions that are similar to Eqs. (22) and (23) can be obtained, i.e.:

$$\Phi_p(\boldsymbol{k},\omega) = \phi_p(\omega)(U_c/\omega)^2 f(\tilde{k}_1, \tilde{k}_3),$$

where $$\phi_p(\omega) \approx \rho^2 u_*^4 \omega^{-1} (\omega\delta_*/U_\infty)^3 [\alpha_p^2 + (\omega\delta_*/U_\infty)^2]^{-3/2}, \tag{30}$$

$$\begin{aligned} f_{chase87}(\tilde{k}_1^2, \tilde{k}_3^2) = {} & \frac{U_c}{u_*}(\omega\delta_*/U_\infty)^{-3}[\alpha_p^2 + (\omega\delta_*/U_\infty)^2]^{3/2}[\beta^2(1-\tilde{k}_1)^2 + \tilde{k}^2 + (b\omega\delta/U_c)^{-2}]^{-5/2} \\ & \text{x} \left[C_M \tilde{k}_1^2 \frac{\tilde{k}^2}{\left|\tilde{k}^2 - \tilde{k}_o^2\right| + \varepsilon^2 \tilde{k}_o^2} + C_T \tilde{k}^2 S \frac{\beta^2(1-\tilde{k}_1)^2 + k^2 + (b\omega\delta/U_c)^{-2}}{\tilde{k}^2 + (b\omega\delta/U_c)^{-2}} \right] \end{aligned} \tag{31}$$

and where $S = c_1 + c_2 \dfrac{\left|\tilde{k}^2 - \tilde{k}_o^2\right|}{\tilde{k}^2} + c_3 \dfrac{\tilde{k}^2}{\left|\tilde{k}^2 - \tilde{k}_o^2\right| + \varepsilon^2 \tilde{k}_o^2}$, $\beta = \dfrac{U_c}{3u_*}$, $\varepsilon = (\pi / 2k_o L_p)^{1/2}$, $\alpha_p \approx 0.12$, u_* is the friction velocity, $\tilde{k}^2 = \tilde{k}_1^2 + \tilde{k}_3^2$, L_p= length of the plate, C_M=0.1553, C_T=0.0047, b=0.75, k_o=ω/c, c_1=2/3, and c_2=c_3=1/6.

The normalized Chase spectrum, $f(\tilde{k}_1^2, \tilde{k}_3^2)$, is not only a function of the normalized wavenumbers, $(\tilde{k}_1^2, \tilde{k}_3^2)$, but also the Strouhal number, $\omega\delta / U_\infty$. The Strouhal number dependency becomes insignificant when $\omega\delta / U_\infty >> 1$, or $\omega\delta_* / U_\infty > 0.5$. The corresponding form of Eq. (31) for the earlier Chase model published in 1980 can be expressed as

$$f_{chase80}(\tilde{k}_1^2, \tilde{k}_3^2) = \frac{U_c}{u_*} \left\{ \begin{aligned} & c_M \tilde{k}_1^2 [\beta^2(1-\tilde{k}_1)^2 + \tilde{k}^2 + (b_M \omega\delta/U_c)^{-2}]^{-5/2} \\ & + c_T \tilde{k}^2 [\beta^2(1-\tilde{k}_1)^2 + k^2 + (b_T \omega\delta/U_c)^{-2}]^{-5/2} \end{aligned} \right\} \tag{32}$$

where $b_M \approx 0.756$ and $b_T \approx 0.379$. The acoustic domain of the wavenumber components are not included in this earlier model. As will be seen in the later discussion, the low-wavenumber spectrum predicted from this model is considerably lower than Chase's 1987 spectrum.

Chase's spectra has been approximately expressed in a way similar to Corcos' wavevector-frequency spectrum, i.e., $\Phi_p(k,\omega) = \phi_p(\omega)(U_c/\omega)^2 f(\tilde{k}_1, \tilde{k}_3)$, and therefore the integrated sum of $f(\tilde{k}_1, \tilde{k}_3)$ with respect to wavevector $(\tilde{k}_1, \tilde{k}_3)$ should be unity. Numerical evaluations indicate that Eqs. (31) and (32) satisfy this requirement. This is an attractive feature for comparing the various spectral models (how the fluctuating energies are distributed to the various wavenumber regions), as their sums of energies are identical. It is also interesting to compare the normalized spectra derived from the Corcos and Chase-1987 models. The Chase spectra are plotted by assuming δ=1 inch, $u_* = 0.032U_\infty$ and $\omega\delta / U_\infty = 10$ (or $U_\infty = 15.5\, m/s$ at 1 *m* from leading edge on a flat plate and at 1000 Hz). Fig. 2 shows the comparison between two spectra plotted in linear scale over the wavevector plane. Both models show the fluctuating energies are concentrated around the convective ridge and are virtually vanishing outside this region. The only differences, in this case, between the two models are how the wavenumber contents are distributed around the ridge: The Chase-1987 spectrum is more concentrated around the ridge while Corcos' spectrum is more spread out. This shows that, in the first order sense, when both the spectrum and wavenumber are plotted in linear scale the wavenumber spectra outside the convective ridge region are insignificant. The quantities of hydroacoustic interest (the low-wavenumber regions) are obviously the second order effects of hydrodynamics.

When the spectral densities are plotted in logarithmic scale (see Fig. 3), the differences in the distribution of energy in the various regions of the wavevector plane are now evident. The Corcos spectrum spreads out more evenly to all regions and has a relatively lower convective ridge but a higher spectral density throughout the wavevector plane including the low-wavenumber region outside the ridge. The Chase spectrum is more concentrated around convective ridge and spreads out less to other regions and has a relatively lower spectral density throughout the wavevector plane including the low-wavenumber region. In a small region near the origin of the wavevector plane, i.e., the region $\omega/c < k < 1/\delta$, the Chase spectrum diminishes rapidly toward small values (proportional to k^2 according to Kraichnan-Phillips Theorem) and the spectral surface displays a tiny but sharp dent in the linear wavevector plane. This tiny region, however, usually contains most of the bending wavenumbers of marine structures. The TBL wall pressure components contained in this small region, $\omega/c < k < 1/\delta$, are therefore the most important source of structural excitations.

When this region is plotted in a logarithmic wavenumber scale (as is usually done in acoustics), the wavenumber axis can be widened to several decades. It is useful to compare the normalized spectra derived from the Corcos, Chase-1980, and Chase-1987 models all together (see Fig. 4) in the commonly used log-log scales for both the spectral levels and wavenumbers. There are two plots shown in the figure: one is the spectral levels as a function of k_1 as k_3 is set equal to zero, the other is the spectral levels as a function of k_3 as k_1 is set equal to zero. The differences in the low-wavenumber regions of both k_1 and k_3 are quite dramatic among the three models when they are compared in the log-log scales. Most of the spectral plots that appear in the literature, similar to Fig. 4, are concerned mainly with the k_1 variations at a fixed k_3, and in most cases, k_3=0. The

k_3 variations are also very important to correctly determine the response of a finite pressure sensor to a TBL pressure field. Based on the data extracted from Smol'yakov and Tkachenko (1991, Figs. 4 & 5), the wavenumber region where the Chase-1987 model is supported by experimental data is also indicated in the figure.

From a modeling perspective, the Chase-1987 model is a hydroacoustically sensible model based on real world experience in hydroacoustics and is consistent with the Kraichnan-Phillips theorem. The Corcos model, on the other hand, was not focused on the secondary hydrodynamic effect and may be considered as a hyrdoacoustically blind model. It should be also remarked that Corcos (1964) did recognize that Kraichnan-Phillips theorem must be satisfied at zero wavenumber. Considering the initial purpose of the correlation measurements was intended for the study of the structure of turbulent flow, Corcos's low wavenumber spectrum may be negligibly small for that purpose. In fact, when the spectrum is displayed in linear scale, there is no visible spectrum at zero wavenumber (see Fig. 2).

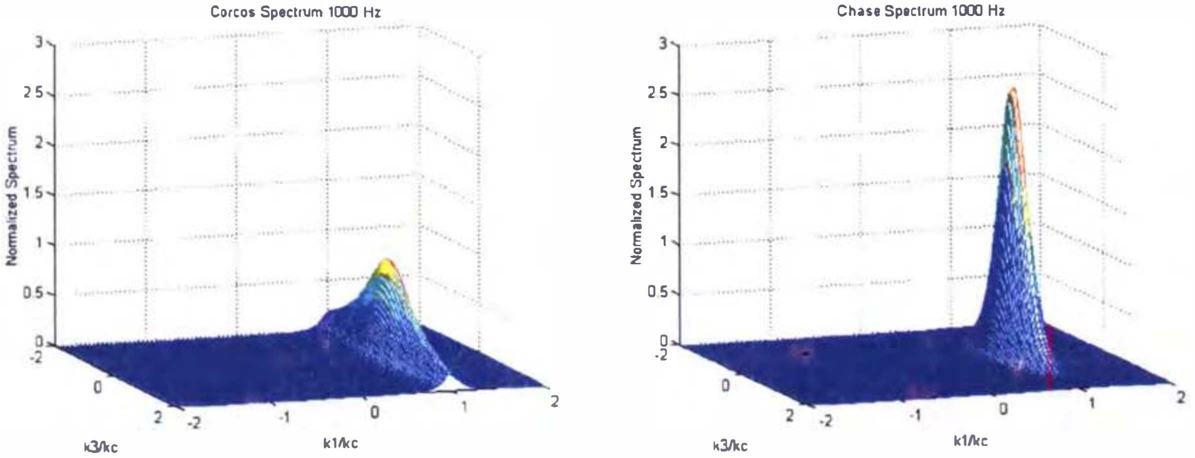

(a) Corcos spectrum

(b) Chase spectrum ($\omega\delta/U_\infty$=10)

Figure 2. Corcos's and Chase's Normalized Spectra Plotted in the Linear Spectral and Wavenumber Scales

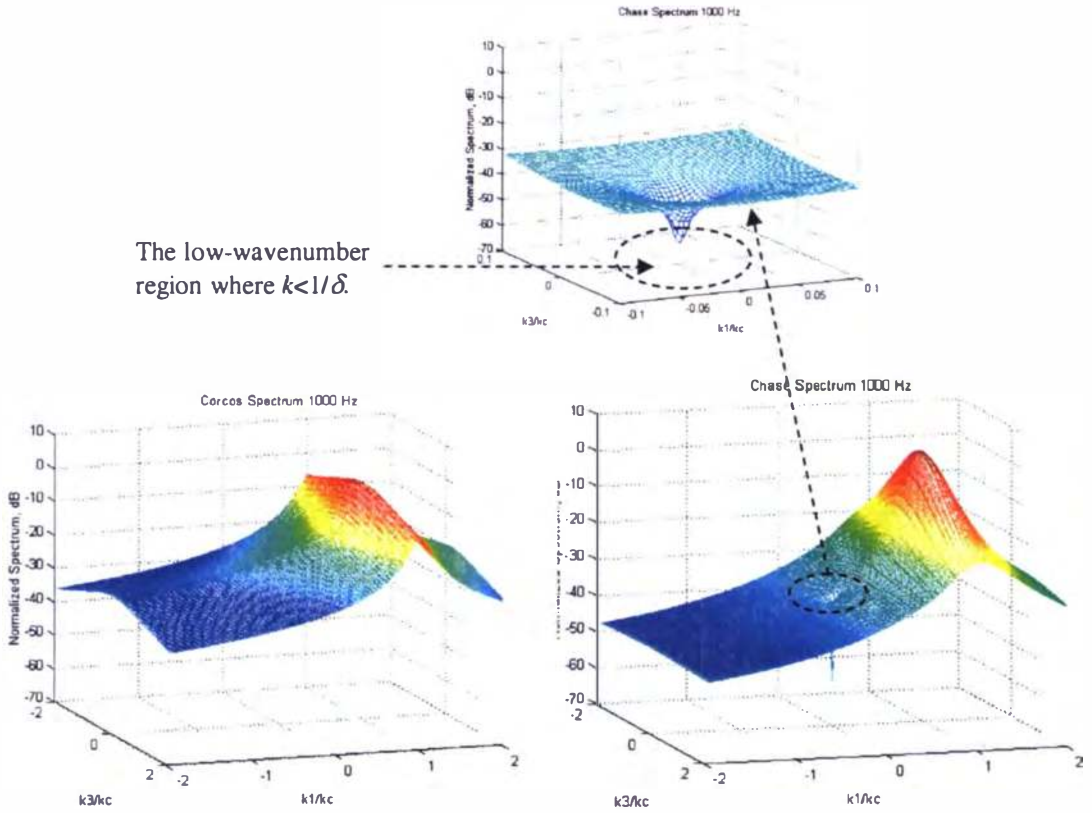

(a) Corcos spectrum

(b) Chase spectrum ($\omega\delta / U_{\infty} = 10$)

Figure 3. Corcos' and Chase's Normalized Spectra Displayed as Logarithmic Spectra as a Function Linear Wavenumbers.

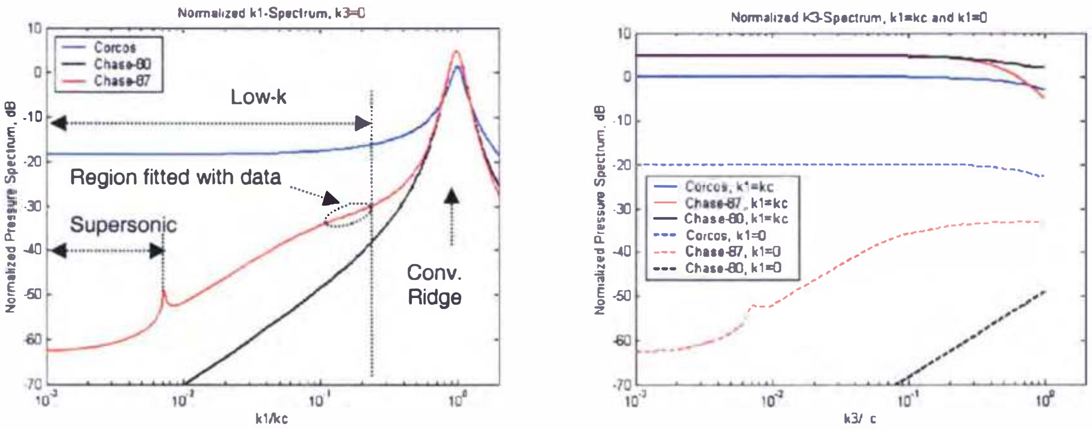

Figure 4. Normalized Corcos's, Chase-1980 and Chase-1987 Spectra Displayed as Logarithmic Spectra as a Function of Logarithmic Wavenumbers in k_1 and k_3.

2.5 Witting and Smol'yakov-Tkachenko Spectra

Although most of the leading theorists accept the so-called Kraichnan-Philips theorem and low-wavenumber constraints, there is no experimental evidence to support it. The experimental data of the low-wavenumber spectra tend to support the low-wavenumber-white spectrum with non-vanishing spectral value at zero wavenumber. This stimulates the several empirical models developed in the 1980's and 1990's. For examples: Efimtsov (1982), Witting (1986), Smol'yakov and Tkachenko (1991), Chase (1987, 1991, 1993), and the Modified Corcos models used by Ko and Schloemer (1989), Hwang (1998), Hambric and Hwang (2000), and a number of others. Efimtsov's model will not be discussed further here since it has been thoroughly examined by Graham (1997) and found to provide insignificant improvement over the original Corcos model.

2.5.1 Witting's Spectrum

Based on the stochastic model of turbulent burst/sweep events, Witting (1986) provided one of the earliest attempts to develop a wavenumber-white model. Witting considered each burst and sweep an independent event and as a dipole that moves with the local mean flow. He derived a Bernoulli relationship that connects the wall fluctuating pressure from an individual event to the fluctuating velocity. Based on the Fourier transforms of the event, he assumed a form of wall pressure wavevector-frequency spectrum contributed by the fluctuating velocity at a distance, d, from the wall:

$$\Phi_p^d(k_1,k_3,\omega) = B\frac{<p^2>}{\rho^2}\frac{d^3}{U_c}\frac{(\omega+k_1U_\infty)^2d^2}{U_c^2}e^{-kd}e^{-2C|\omega/U_c+k_1|d}$$

where $< p^2 >$ is the mean square pressure, B is a dimensionless constant, and C is an arbitrary constant. The wavenumber-frequency spectrum is then obtained by summing the above spectrum over a range d, according to an assumed probability density function, i.e., $\Pr(d) \propto 1/d$. Finally, the wavevector-frequency spectrum which is result of the integrated sum of the dipole contributions, between the inner scale $\delta_{\min}$ and outer scale $\delta_{\max}$, is shown below:

$$\Phi_p(k,\omega) = < p^2 > \frac{\delta_*^3}{U_c}\frac{A\hat{\omega}^2}{\xi^5}\frac{8}{3}\{(x^4/2+x^3+3x^2/2+3x/2+3/4)e^{-2x}\}\Big|_{\xi_{\min}}^{\xi_{\max}} \tag{33}$$

where $\xi = \hat{k} + C\left|\hat{\omega} - \hat{k}_1\right|$; $\xi_{\max} = (\delta_{\max}/\delta_*)\xi$; $\xi_{\min} = (\delta_{\min}/\delta_*)\xi$; $\hat{k}_1 = k_1\delta_*$; $\hat{k}_3 = k_3\delta_*$;

$$\hat{k} = \sqrt{\hat{k}_1^3 + \hat{k}_3^3}\,;\ \hat{\omega} = \omega\delta_*/U_c;\ A = C/\{\pi[1+2/(3C^2)]\ln(\delta_{\max}/\delta_{\min}\};$$

$$< p^2 >= \int_{-\infty}^{\infty} dk_1 \int_{-\infty}^{\infty} dk_3 \int_{-\infty}^{\infty} d\omega\Phi_p(k,\omega) \approx 0.015\rho^2U_c^2u_*^2\,.$$

This leads to a low-wavenumber white spectrum and the level can be made to fit the experimental data with a proper choice of C (the value C=8 is recommended by Witting). Witting's formulation was, however, criticized as artificially introducing a volume dipole

(Dowling, 1998), which is incompatible with the equations of motion (the incompressible Lighthill equations).

Witting's frequency spectrum is then the integrated sum of Eq. (33) over the wavevector plane:

$$\phi_p(\omega) = \frac{(16/3) < p >^2 A}{C|\omega|} \int_{\omega\delta_{\min}/U_c}^{\omega\delta_{\max}/U_c} x^3 K_1(2x)dx \tag{34}$$

and, the dimensionless form of Witting's wavenumber spectrum is then

$$f_{Witting}(\tilde{k}_1, \tilde{k}_3) = \frac{C(\omega\delta_* / U_c)^5 \xi^{-5} \{(x^4/2 + x^3 + 3x^2/2 + 3x/2 + 3/4)e^{-2x}\}\Big|_{\xi_{\min}}^{\xi_{\max}}}{2\int_{\omega\delta_{\min}/U_c}^{\omega\delta_{\max}/U_c} x^3 K_1(2x)dx} \tag{35}$$

where $\hat{k}_1 = (\omega/U_c)\tilde{k}_1\delta_*$, and $\hat{k}_3 = (\omega/U_c)\tilde{k}_3\delta_*$. As shown in Fig. 5, Witting's low-wavenumber spectrum is about 15 dB lower than that of Corcos's but the convective ridge level is much higher, indicating a shift of spectral energy toward the convective ridge. Witting's frequency spectrum will be discussed later along with the other models.

2.5.2 Smol'yakov-Tkachenko Spectrum

Smol'yakov and Tkachenko (1991) discussed the inadequacy of the Corcos model for predicting the low-wavenumber spectra. Based on their measurements of the longitudinal and lateral correlations at a large range of spacing, e.g., $\xi_1/\delta_* = 2.6 \rightarrow 52.0; \xi_3/\delta_* = 2.3 \rightarrow 9.6$, they argued that the deviations from similarity with respect to $\omega\xi_1/U_c$ and $\omega\xi_3/U_c$ increase as ξ/δ_* increases. Therefore, they proposed to use frequency dependent generalized decay rates, $\bar{\alpha}(\omega)$, in conjunction with a non-rectangular product form of the coherence function:

$$C(\omega\xi_1/U_c, \omega\xi_3/U_c) = \exp[-\bar{\alpha}(\omega)\sqrt{(\omega\xi_1/U_c)^2 + m_o^2(\omega\xi_3/U_c)^2} + i\omega\xi_1/U_c] \tag{36}$$

where $\bar{\alpha}(\omega) = \alpha_1\sqrt{1 - 0.2(\omega\delta_*/U_c)^{-1} + 0.2^2(\omega\delta_*/U_c)^{-2}}$ and m_o is the ratio of the spanwise and streamwise decay rates, i.e., $m_o = \alpha_3/\alpha_1$ (≈ 6.45). This coherence function is now an exponential function of the square root of the geometric sum of streamwise and spanwise distances. The frequency dependency of the generalized decay rate is more significant at small values of $\omega\delta_*/U_c$ while $\bar{\alpha}(\omega) \rightarrow \alpha_1$ at large values of $\omega\delta_*/U_c$.

Using the relationships $\int_0^\infty e^{-\alpha\sqrt{x^2+y^2}} \cos(bx)dx = \frac{\alpha y}{\sqrt{\alpha^2 + b^2}} K_1(y\sqrt{\alpha^2 + b^2})$ and

$\int_0^\infty yK_1(cy)\cos(gy)dy = \frac{\pi}{2}c(c^2+g^2)^{-3/2}$ (Gradshteyn & Ryzhik, 1965; pages 482 and 749, respectively), Smol'yakov-Tkachenko's dimensionless Spectrum can be obtained in a rather simple form as follows:

$$f_{S\&T}(\tilde{k}_1,\tilde{k}_3) = \frac{\bar{\alpha}}{2\pi m_o}\left[\bar{\alpha}^2 + (1-\tilde{k}_1)^2 + (\tilde{k}_3/m_o)^2\right]^{-3/2} \tag{37}$$

Their $\Phi_p(\boldsymbol{k},\omega)$ at zero and convective wavenumbers, is then approximately,

$$\Phi_p(\boldsymbol{k},\omega) \approx \phi_p(\omega)\left(\frac{U_c}{\omega}\right)^2 \begin{cases} \alpha_1\bar{\alpha}/2\pi\alpha_3, & (k_1,k_3)\to(0,0) \\ \alpha_1/2\pi\bar{\alpha}^2\alpha_3, & (k_1,k_3)\to(k_c,0) \end{cases}.$$

When this is compared to the Corcos spectrum, Smol'yakov-Tkachenko's zero wavenumber spectrum is lower by the factor of $\pi\bar{\alpha}/2$, which is about 8 dB lower when the value of $\bar{\alpha}$ is assumed to be 0.1. Smol'yakov and Tkachenko considered this was still too high as compared to the measured low-wavenumber spectra, so they introduced a correction factor, which has similar low-wavenumber characteristics as Eq. (37) but will not yield an significant high wave number components:

$$\Delta f(\tilde{k}_1,\tilde{k}_3) = \frac{\bar{\alpha}}{2\pi m_o}\frac{1}{n}\left[1+\bar{\alpha}^2+\frac{n}{m_1}(m_1-\tilde{k}_1)^2+\tilde{k}_3^2-m_1^2\right]^{-3/2}$$

where $m_1 = (1+\bar{\alpha}^2)/(5n-4+\bar{\alpha}^2)$ and n is a constant chosen to fit measured data. The final form of the normalized wavevector-frequency spectrum is

$$f_{S\&T}(\tilde{k}_1,\tilde{k}_3) = \frac{\bar{\alpha}}{2\pi m_o}h(\omega)\left[f(\tilde{k}_1,\tilde{k}_3) - \Delta f(\tilde{k}_1,\tilde{k}_3)\right] \tag{38}$$

If n is chosen to be near unity, the values of $f(\tilde{k}_1,\tilde{k}_3)$ and $\Delta f(\tilde{k}_1,\tilde{k}_3)$ at low-wavenumbers are very close and the difference is therefore is a small value. For example, if n=1.005 as suggested by Smol'yakov and Tkachenko, $f(\tilde{k}_1,\tilde{k}_3) - \Delta f(\tilde{k}_1,\tilde{k}_3) \approx 0.005 f(\tilde{k}_1,\tilde{k}_3)$, and the corrected spectrum will be about 23 dB lower than the uncorrected spectrum. Due to the coherence function expressed as an exponential function of the square root of the geometric sum of streamwise and spanwise separations, Smol'yakov and Tkachenko's k_3-spectrum is now similar to that of Chase's showing an increase in value with wavenumber rather than a slight decrease in value with wavenumber in the Corcos' and Witting's spectra.

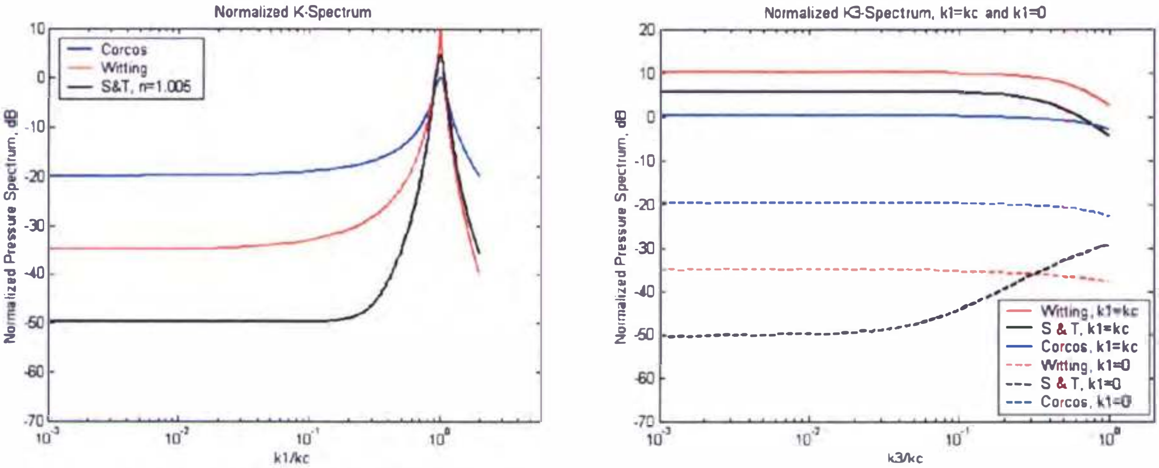

k_1 spectrum (k_3=0) k_3 spectrum (k_1=0)

Figure 5. Normalized Corcos's, Witting's and Smol'yakov-Tkachenko's Spectra Displayed in Logarithmic Spectra as a Function of Logarithmic Wavenumbers.

2.6 Modifications of the Corcos Model

As mentioned earlier, the Corcos model of cross spectral density function is an approximate model derived from the results of two-point correlation measurements. This spectrum is applicable primarily in the region that is dominated by the convected pressure field. In the low wavenumber region of vibroacoustic interest, Corcos's wavenumber-frequency spectrum has been shown to be inaccurate. Because Corcos' cross-spectral density function was derived from experimental data with the appeal of simplicity, the reason for its inaccuracy at low wavenumbers will be examined first, and then the possible remedial modifications to improve its accuracy will be investigated.

From the definition of Fourier transform, Eq. (21), the wavevector-frequency spectrum for Eq. (18) at zero streamwise and spanwise wavenumber is equal to $\phi_p(\omega)$ times the product of two integrals; the first is the integration of $A(\omega\xi_1/U_c)\exp(i\omega\xi_1/U_c)/2\pi$ with respect to ξ_1, and the second is the integration of $B(\omega\xi_3/U_c)/2\pi$ with respect to ξ_3. The integration limits for both are from $-\infty$ to ∞. It is noted that the factor, $\exp(i\omega\xi_1/U_c)$, is required for the streamwise cross spectrum to account for the effect of the mean convection of the flow. No such factor is required for the spanwise cross spectrum. Therefore, if Eq. (18) is determined by a pairs of measuring sensors mounted in the convected frame of reference, the factor $\exp(i\omega\xi_1/U_c)$ in the first integrand must be dropped, because there would be no mean convection effect on the sensors. In other words, the streamwise cross-spectrum measured by the moving sensors would be similar to the spanwise cross-spectrum measured by pairs of stationary sensors except for the differences in decay rates. In this case, the calculated spectrum will peak at zero wavenumber, which is proportional to the product of the areas under $A(\omega\xi_1/U_c)\ B(\omega\xi_3/U_c)/(2\pi)^2$ and is equal to $\phi_p(\omega)(U_c/\omega)^2/(\pi^2\alpha_1\alpha_3) = \phi_p(\omega)\ell_1\ell_3/\pi^2$ where $\ell_1\ell_3$ is the correlation area. Therefore, the net force spectrum per unit area exerted by a TBL on a rigid plate is proportional to the correlation area only when the plate is convected with the flow. When the measuring sensors are mounted in the fixed frame of reference, the spectral peak is shifted to the convective wavenumber due to the factor $\exp\left(i\omega\xi_1/U_c\right)$. The convective ridge spectrum is then equal to $\phi_p(\omega)\ell_1\ell_3/\pi^2$. However, the frequency spectrum $\phi_p(\omega)$ observed in the convected frame could be much less, because in a completely frozen flow there is no time-varying signature which can be observed in the convected frame of reference (Fisher and Davies, 1963).

The zero wavenumber spectrum observed in a fixed frame of reference, on the other hand, is proportional to the integration of $A(\omega\xi_1/U_c)\cos\left(\omega\xi_1/U_c\right)/2\pi$ with respect to ξ_1. The function A is symmetric in $\omega\xi_1/U_c$. Fig. 6 shows the integrand, $A(\omega\xi_1/U_c)\cos\left(\omega\xi_1/U_c\right)$, plotted as a function of $\omega\xi_1/U_c$ (the red curve). The zero wavenumber spectrum is now equal to the integrated sum of $A(\omega\xi_1/U_c)\cos\left(\omega\xi_1/U_c\right)/2\pi$ with respect to ξ_1 times $\phi_p(\omega)(U_c/\omega)\ /(\pi\ \alpha_3)$. Noting that $A(\omega\xi_1/U_c)=exp(-\alpha_1\omega|\xi_1|/U_c)$ is a steady decaying function and $\cos\left(\omega\xi_1/U_c\right)$ is a rapidly oscillating function of ξ_1, the resulting integral of the product is a small value which is proportional to the decay rate. The non-zero spectrum at k_1=0 is contributed by the residue of incomplete sinusoidal cancellation due to the spatial decay of coherence; the smaller the decay rate the smaller the spectrum at k_1=0. The net value of the integrated sum of $A(\omega\xi_1/U_c)\cos\left(\omega\xi_1/U_c\right)/2\pi$ is shown to be equal to $(U_c/\omega)\alpha_1\ /[\pi(1+\alpha_1^2)] \equiv (U_c/\omega)\alpha_1\ /\pi$ since $\alpha_1 << 1$. The ratio between the integrated values with and without the oscillating term is then approximately equal to $[\,(U_c/\omega)\alpha_1\ /\pi\,]/\,[\,(U_c/\omega)/(\pi\alpha_1)\,]=\alpha_1^2$. Since $\alpha_1\ \equiv 0.1$, the effect of the oscillating term thus reduces the streamwise integral to about 1%. Therefore the zero wavenumber spectrum is actually very small, but is still too large in aero and hydro acoustics. The spectrum of the net force exerted on a stationary rigid plate will be proportional to the plate area times $\phi_p(\omega)\alpha_1^2\ell_1\ell_3/\pi^2$ in contrast to that times $\phi_p(\omega)\ell_1\ell_3/\pi^2$ when the plate is convected with the flow. The factor α_1^2 (the ratio of the zero wavenumber and convective-wavenumber spectra) is often incorrectly ignored in predicting the TBL exerted force on a stationary finite plate when the correlation area is used.

Corcos's zero wavenumber level is about one percent of the convective ridge level. This may be negligibly small from a fluid dynamics point of view. However, a problem arises when it is used as the forcing function for a large structure. Because a large structure acts as an enormous low-pass wavenumber filter and demands a more accurate low-wavenumber spectrum. This accuracy is inherently impossible to obtain from Corcos' simple model, which is based on correlation measurements dominated by the pressure fluctuations convected with the flow. A more accurate low-wavenumber spectrum might be obtained if one could actually conduct the space-time correlation according Eq. (12). The Fourier transform of this function would ensure that its wavenumber and frequency contents are orthogonal under the area and time averaging process. Since a direct measurement of the space-time correlation function is not possible, the exact value of the low-wavenumber spectrum is not known. We can only estimate this spectrum using a mathematical model based on the response of a mechanical system such as a flat plate or an array of pressure sensors; both systems respond instantaneously to the space averaged TBL forces at any instance of time. From reported measurements by Martin and Leehey (1977), Farabee and

Geib (1976), and others, the Corcos's low wavenumber spectrum must be reduced in the order of 20 dB. Some modifications of the Corcos-type spectrum for predicting the low-wavenumber spectra to be more inline with the measured data are discussed as follows.

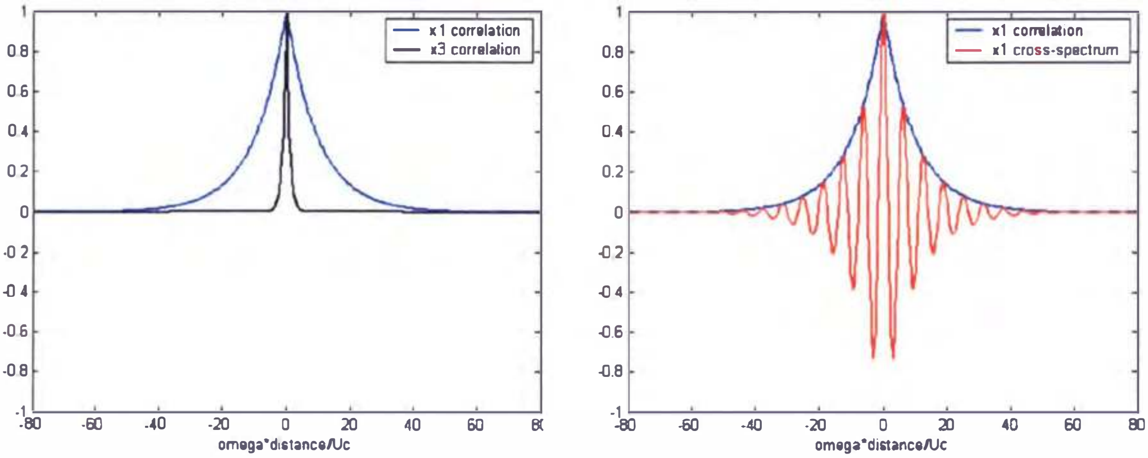

(a) Streamwise and spanwise correlations (b) Streamwise cross-spectrum (red curve)

Figure 6. Corcos's correlation functions and the streamwise Cross-Spectrum

2.6.1 Ko and Schloemer Spectrum

Since Corcos's low wavenumber spectrum is about 20 dB below the convective ridge and is about 20 dB too high, the rule of dumb is that the correct low wavenumber spectrum must be about 40 dB below the convective ridge. One simple way to accomplish this is by reducing the value of α_1 from its typical value of 0.1 to 0.01 (Ko and Schloemer, 1992) while keeping α_3 unchanged. According to Eq. (24), this will reduce the Corcos's zero wavenumber spectrum by 10 dB while increasing the convective ridge by 10 dB, and consequently the zero wavenumber spectrum is about 40 dB below the convective ridge. Ko and Schloemer's simple modification of the Corcos spectrum was aiming at an acceptable low wavenumber spectrum, since the accuracy of the high wavenumber spectrum was not important in their analysis. Comparing convective ridge levels shown in Fig. 4, the Chase spectrum is about 5 dB higher than the Corcos spectrum, and the Ko and Schloemer's modified spectrum is another 5 dB higher still. Using this modified wavenumber spectrum in conjunction with a simple Strouhal scale independent frequency spectrum, $\phi_p(\omega) = \rho^2 u_*^4 \omega^{-1}$, Ko and Schloemer indicated that their calculations of the flow noise reduction for a planar array of hydrophones were satisfactory.

2.6.2 Willmarth and Roos Spectrum

At the time the Corcos model was proposed, correlation of wall pressure for very small spatial separation, say $|\xi_1| < 0.7\delta_*$, had not been measured due to the limitation of finite size pressure sensors. Corcos's similarity of the cross-spectral density function assumed this missing information. In wavenumber-frequency domain analysis, Willmarth and Roos [1965] attempted to recover the TBL power spectrum that would be measured by a point transducer from correcting the data measured by a finite size transducer. They believed that the missing information at small spatial separation might be crucial for accurately determining the correction factor, especially at low frequencies. Accordingly, Corcos's coherence functions are modified as shown below to improve the fit between prediction and measured data:

$$A(\tilde{\xi}_1) = \exp(-\alpha_1 |\tilde{\xi}_1|) + \alpha_1 |\tilde{\xi}_1| \exp(-b_1\alpha_1 |\tilde{\xi}_1|) \tag{39a}$$

$$\begin{aligned} B(\tilde{\xi}_3) &= 0.155\exp(-0.092|\tilde{\xi}_3|) + \alpha_3 \exp(-0.789|\tilde{\xi}_3|) \\ &\quad + 0.145\exp(-2.916|\tilde{\xi}_3|) + 1.414\alpha_3 |\tilde{\xi}_3| \exp(-b_3\alpha_3 |\tilde{\xi}_3|) \end{aligned} \tag{39b}$$

where $\tilde{\xi}_1 = \omega\xi_1/U_c$, $\tilde{\xi}_3 = \omega\xi_3/U_c$, α_1=0.1145, b_1=21.83, α_3=0.7, and b_3=5.71. The last term on the right-hand-side of Eqs. (39a) and (39b) were chosen to make $A'(0)$ and $B'(0)$ zero while the corresponding terms of Corcos's original function have negative slopes at the origin. This is likely the first time the Corcos cross-spectrum was modified. The decay constants in the added terms increase the values of both coherences, A and B. Eq. (39a) predicted streamwise coherence agrees well with the measured data and that predicted by the original Corcos function, except a small notable change when $\tilde{\xi}_1 < 1$. The spanwise coherence shown by Eq. (39b), agrees well with measured data, while the original Corcos function predicts a considerably lower value when $\tilde{\xi}_3$ >2 (Willmarth and Roos, 1965, Figs. 1 and 2; Farabee, 1986, Fig. 5.11) .

In order to obtain a similar normalized wavenumber spectrum shown in Eq. (23), Willmarth and Roos's normalized spectrum is denoted as

$$f_{W\&R}(\tilde{k}_1, \tilde{k}_3) = f_1(\tilde{k}_1) f_3(\tilde{k}_3) \tag{40}$$

where the subscript $W\&R$ indicates that the spectrum is the result of Fourier transform of the Willmarth and Roos coherence functions. Consequently,

$$\begin{aligned} f_1(\tilde{k}_1) &= \frac{\alpha_1}{\pi}\left\{\frac{1}{\alpha_1^2 + (1-\tilde{k}_1)^2} + \frac{(b_1\alpha_1)^2 - (1-\tilde{k}_1)^2}{[(b_1\alpha_1)^2 + (1-\tilde{k}_1)^2]^2}\right\}, \\ &= \frac{\alpha_1^3(3b_1^2 - 1)(1-\tilde{k}_1)^2 + b_1^2(1+b_1^2)\alpha_1^5}{\pi[\alpha_1^2 + (1-\tilde{k}_1)^2][(b_1\alpha_1)^2 + (1-\tilde{k}_1)^2]^2} \end{aligned} \tag{41}$$

and

$$\begin{aligned} f_3(\tilde{k}_3) &= 0.155\left\{\frac{0.092}{\pi\left[0.092^2 + (\tilde{k}_3)^2\right]}\right\} + \alpha_3\left\{\frac{0.789}{\pi\left[0.789^2 + (\tilde{k}_3)^2\right]}\right\} \\ &\quad + 0.145\left\{\frac{2.916}{\pi\left[2.916^2 + (\tilde{k}_3)^2\right]}\right\} + 1.414\alpha_3\left\{\frac{(b_3\alpha_3)^2 - (\tilde{k}_3)^2}{\pi\left[(b_3\alpha_3)^2 + (\tilde{k}_3)^2\right]^2}\right\} \end{aligned} \tag{42}$$

The last terms on the right-hand-side of the above two equations are the Fourier transforms of the last terms on the right-hand-side of Eqs. (39a) and (39b). These terms were intended by Willmarth and Roos to make the coherence functions have zero slope at the origin in order to reduce the undesirable high wavenumber components. The normalized spectrum of Eqs. (41) and (42) will be called the Willmarth-Roos spectra. As shown in Fig. 7, the differences between this spectrum and that of Corcos' are not particular significant except at the convective ridge region, the k_3-variations in particular. The main difference is that Willmarth-Roos's spanwise wavenumber spectra near the convective ridge is more concentrated (with a hump contributed by the first term in Eq. (39b)) at $k_3=0$, while Corcos's spectrum spreads out more evenly. This causes Willmarth-Roos spectrum to have a higher convective ridge. Similar spectral curves of the Chase-87 spectrum are also shown in the figure, which shows a significant departure from Corcos's and Willmarth-Roos's spectra especially in the low wavenumber region. Incidentally, Willmarth-Roos's convective ridge matches perfectly with that of Chase-87. This may justify the modification by Willmarth-Roos to improve the prediction of sensor attenuation near the convective ridge. However, Willmarth-Roos's low k_3 spectrum (when $k_1=0$) shows a small hump at $k_3=0$ instead of a dip that is shown in the Chase's physics based spectrum. Therefore, the modification of the spanwise coherence, Eq. (39b), is considered to be unnecessary for the purpose of improving the low wavenumber spectrum of Corcos. Corcos's original form, Eq. (20) should be used instead.

The last terms of Eq. (39a) and (39b) produce a negative spectrum when

$$\tilde{k}_1 < (1-b_1\alpha_1),\ \tilde{k}_1 > (1+b_1\alpha_1) \text{ and } \left|\tilde{k}_3\right| > b_3\alpha_3$$

where $b_1\alpha_1$ and $b_3\alpha_3$ are the exponential decay factors. These terms reduce the wavenumber spectra produced by the respective preceding terms. For example, the first term of Eq. (39a) is the Corcos approximated streamwise coherence function, which is responsible for the unwanted high low wavenumber spectrum. The second term may help to reduce it. Since Willmarth and Roos's $b_1\alpha_1$ and $b_3\alpha_3$ are equal to 2 and 4, respectively, the negative spectra will occur when $\tilde{k}_1 < -1$, $\tilde{k}_1 > 2$ and $\left|\tilde{k}_3\right| >4$. These wavenumbers are outside the low wavenumber region of interest. From the previous comparison between Corocs and Chase spectra (see Figs 4), it is desirable to reduce Corcos spectrum in the entire wavevector plane outside the convective ridge. This can be done by properly choosing b_1 and b_3. Fig. 8 shows the normalized Willmarth-Roos spectra at the various value of b_1, while b_3 is kept to be equal to 2. It is shown that when b_1 is reduced to 0.5, the Willmarth-Roos's low-wavenumber spectrum will be about 20 dB lower than that of the Corcos spectrum. Therefore, it is remarkable that the modification of the Corcos streamwise coherence function by adding the term, $\alpha_1|\gamma|\exp(-b_1\alpha_1|\gamma|)$, where $\gamma = \omega\xi_1/U_c$, as it was done by Willmarth and Roos can reduce the low-wavenumber spectrum to any desired level by adjusting the value of b_1.

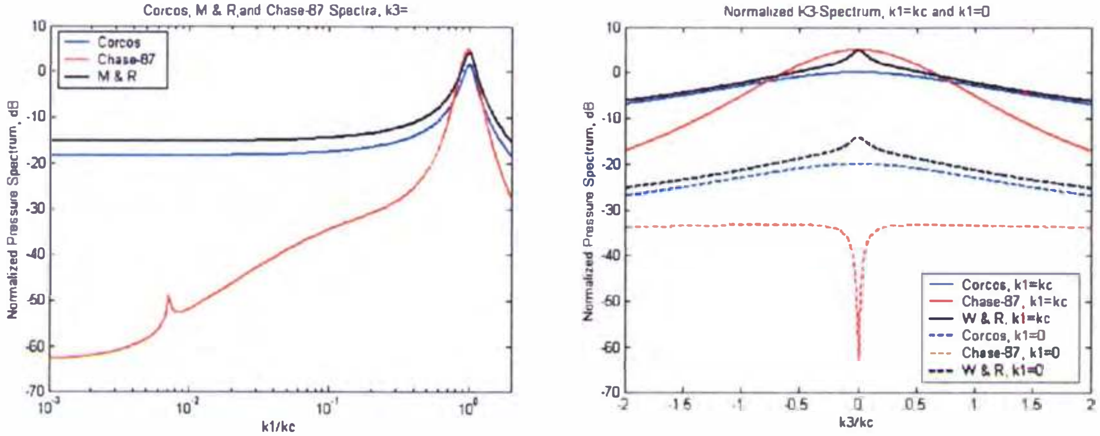

Figure 7. Normalized Corcos's, Chase-87 and Willmarth-Roos Spectra Displayed as Logarithmic Spectra as a Function of Logarithmic Wavenumber in k_1 and Linear Wavenumber in k_3.

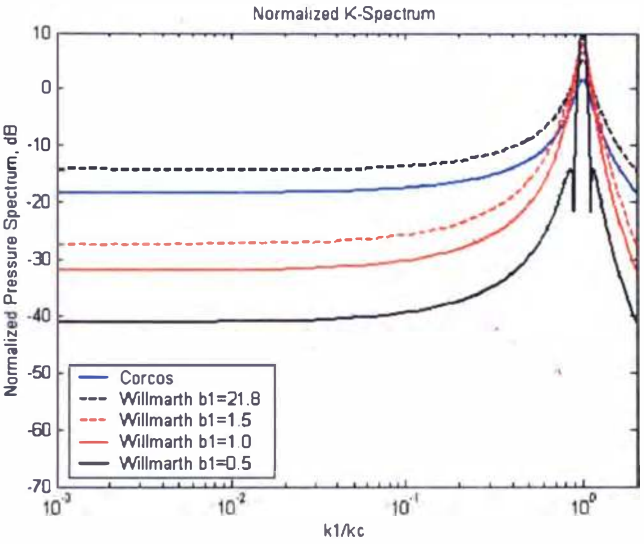

Figure 8. Normalized Corcos and Willmarth-Roos Spectra with Various Values of b_1

2.6.3 Modified Corcos Spectrum

The Modified Corcos cross-spectrum given in this section was suggested by Elswick (1983) of the Naval Undersea Warfare Center, Newport, RI (formerly the Naval Undersea System Center, New London, CT). Some successful applications of this spectrum were reported by Ko (1991), Hwang (1998) and Hambric and Hwang(2000). Since the information on how this model evolved was not known to the authors, a discussion follows on the two sources that may lead to the

Modified Corcos spectrum shown in Eq. (43): the first is Willmarth and Roos's model mentioned in the previous section, the second is Chase's (1987) approximated correlation functions.

In Willmarth-Roos's modified cross-spectrum if the constants b_1 and b_3 are chosen to be 1 and 2 respectively, the last two terms of Eqs. (39a) and (39b) will produce negative values in the wavenumber ranges $\tilde{k}_1 < 0.9$ and $|\tilde{k}_3| > 1.4$. In Fig. 8, the normalized Willmarth-Roos spectrum with $b_3=2$ at various values of b_1 is shown. When b_1 is reduced to 0.5, the Willmarth-Roos's low wavenumber spectrum may be reduced to a desirable level, but there are two irregular kinks on its spectral curve just outside the convective ridge. Therefore, a desirable choice of b_1 may be $b_1=1$. This leads to a simple form of the modified Corcos cross-spectral density function, which is identical to that suggested by Elswick (1983), i.e.,

$$\Gamma_{mc}(\xi,\omega) = \phi_p(\omega)\left(1+\alpha_1|\omega\xi_1/U_c|\right)\exp\left(-\alpha_1|\omega\xi_1/U_c|\right)\exp\left(-\alpha_3|\omega\xi_3/U_c|\right)\exp\left(i\omega\xi_1/U_c\right) \tag{43}$$

where the original Corcos spanwise correlation function is used, and the streamwise correlation function is multiplied by the factor, $1+\alpha_1|\omega\xi_1/U_c|$. This means that the original streamwise correlation is increased proportional to $\alpha_1|\omega\xi_1/U_c|$. Since $\alpha_1 \sim 1/10$, the increase is small at small values of $\omega\xi_1/U_c$. However, the increase becomes significant when $\omega\xi_1/U_c > 10$. Like the Chase-1980 version of the cross-spectral density function, this cross-spectrum is, as expected, significantly different from the typical Corcos type cross spectra obtained from fitting the data from two-point correlation measurements. The increase of correlation thus shifts the spectral contents toward the convective ridge while reducing the low wavenumber spectrum.

As mentioned earlier, there is no corresponding closed form solution of the cross-spectral density function for Chase's 1987 wavevector-frequency spectrum. However, Chase pointed out that in the Strouhal scale independent range, where $\omega\delta/U_\infty >> 1$, the streamwise and spanwise correlations may be approximated by

$$A(\omega\xi_1/U_c) = \left(1+\frac{\mu|\omega\xi_1/U_c|}{1+r_T}\right)\exp(-\mu|\omega\xi_1/U_c|)$$

and

$$B(\omega\xi_3/U_c) = \left(1+\frac{1-r_T}{1+r_T}|\omega\xi_3/U_c|\right)\exp(-|\omega\xi_3/U_c|), \text{ respectively.}$$

The corresponding normalized non-dimensional spectra are then

$$f_1(\tilde{k}_1) = \frac{1}{\pi}\left\{\frac{\mu}{\mu^2+(1-\tilde{k}_1)^2} + \frac{\mu}{1+r_T}\left(\frac{\mu^2-(1-\tilde{k}_1)^2}{[\mu^2+(1-\tilde{k}_1)^2]^2}\right)\right\}$$

and

$$f_3(\tilde{k}_3) = \frac{1}{\pi}\left\{\frac{1}{1+\tilde{k}_3^2} + \frac{1-r_T}{1+r_T}\left(\frac{1-\tilde{k}_3^2}{[1+\tilde{k}_3^2]^2}\right)\right\}.$$

In the low wavenumber and convective ridge limits, the above wavenumber-frequency spectrum approaches the following values:

$$\Phi_p(\boldsymbol{k},\omega) \approx \phi_p(\omega)\left(\frac{U_c}{\omega}\right)^2 \begin{cases} \dfrac{2}{(1+r_T)\pi^2}\left(\dfrac{2\mu^3 + r_T\mu(1+\mu^2)}{(1+r_T)(1+\mu^2)^2}\right), & (k_1,k_3)\to(0,0) \\ \dfrac{2(2+r_T)}{\mu(1+r_T)^2\pi^2}, & (k_1,k_3)\to(k_c,0) \end{cases}$$

With the values $\mu \approx 0.176$ and $r_T \approx 0.389$ recommended by Chase, the zero wavenumber spectrum shown above is about the same as Corcos's spectrum. This approximated form of the correlation function is therefore not capable of generating the desired low wavenumber spectrum.

However, when the value r_T is assumed zero, we have

$$A(\omega\xi_1/U_c) \approx \left(1+\mu\left|\omega\xi_1/U_c\right|\right)\exp(-\mu\left|\omega\xi_1/U_c\right|),$$

and

$$B(\omega\xi_3/U_c) \approx \left(1+\left|\omega\xi_3/U_c\right|\right)\exp(-\left|\omega\xi_3/U_c\right|).$$

This streamwise correlation will have the same form as that of the modified Corcos model. However, in this case, the spanwise correlation is also similarly modified. Therefore, the Modified Corcos cross-spectrum is somewhat inline with Chase's (1987) approximation.

The Modified Corcos wavevector-frequency spectrum is then the Fourier transform of Eq. (43), which is

$$\Phi_p(\tilde{k}_1,\tilde{k}_3,\omega) = \phi_p(\omega)\left(\frac{U_c}{\omega}\right)^2 \left\{\frac{2\alpha_1^3}{\pi\left[\alpha_1^2 + (1-\tilde{k}_1)^2\right]^2}\right\}\left\{\frac{\alpha_3}{\pi\left[\alpha_3^2 + \tilde{k}_3^2\right]}\right\}, \qquad (44)$$

and the approximate spectrum at zero wavenumber spectrum is

$$\Phi_p(\boldsymbol{k},\omega) \approx \phi_p(\omega)\left(\frac{U_c}{\omega}\right)^2 \left\{\frac{2\alpha_1^3}{\pi^2\alpha_3}\right\} \quad as \ (k_1,k_3)\to 0 , \qquad (45)$$

which is lower than that of the Corcos spectrum by the factor of $2\alpha_1^2$ ($\approx 0.02 = -17dB$). The spectrum at the convective ridge, on the other hand, is doubled (+3 dB). This yields a zero wavenumber spectrum which is about 40 dB below the convective ridge. The above modification does not change the integrated value of the wavenumber spectrum, since the doubling of the values at convective ridge is compensated by the reduction of the wavenumber contents outside the ridge. The spectrum of the net force exerted on a rigid plate calculated from the Modified Corcos spectrum will now be proportional to the plate area times $\phi_p(\omega)2\alpha_1^4\ell_1\ell_3/\pi^2$ in contrast to that times $\phi_p(\omega)\alpha_1^2\ell_1\ell_3/\pi^2$ when the original Corcos spectrum is used. The comparison of this spectrum to the other spectra will be shown in the latter sections.

2.7 Pressure Spectrum Caused by Viscous Shear Stresses

In viscous flows, the Navier-Strokes equations may be linearized in the near wall region and the equations of motion can be separated into irrotational, v_ℓ, and rotational, v_t, components (Morse and Ingard, 1968):

$$\rho\frac{\partial v_\ell}{\partial t} = -\nabla p \quad \text{and} \quad \rho\frac{\partial v_t}{\partial t} = -\mu \text{ curl curl } v_t, \text{ respectively.}$$

On a rigid surface S with normal $\boldsymbol{n}$, in order to satisfy the no slip wall condition, $v_\ell + v_t = 0$, the pressure and shear stress must satisfy the following boundary condition,

$$n\cdot\nabla p = n_i\frac{\partial\sigma_{ij}}{\partial x_j} \qquad \text{on } S. \tag{46}$$

The inviscid solution, Eq. (27), must now include the wall shear stress contributions (Dowling, 1998):

$$p(x,t) = \int_V G(x/y)\frac{\partial^2}{\partial y_i\partial y_j}\rho v_i v_j(y,t)d^3y + \int_S \frac{\partial G(x/y)}{\partial y_i}\sigma_{ij}(y,t)dS_j \tag{47}$$

In the case of an infinite plane surface, G is the half space Green function, Eq. (47) can be simplified to

$$p(x,t) = \frac{1}{2\pi}\int_{V,y>0} |x-y|^{-1}\frac{\partial^2\rho v_i v_j(y,t)}{\partial y_i\partial y_j}d^3y - 2\int_S\frac{\sigma_{\alpha 2}(y,t)}{|x-y|}dy_1 dy_3 \tag{48}$$

where α must be summed over two directions in the plane, 1 and 3. Similar to the way Eq. (29) was obtained, the wavevector-frequency transform of the surface pressure, $P_S(\boldsymbol{k},\omega)$, becomes

$$P_s(\boldsymbol{k},\omega) = \frac{k_i k_j}{|\boldsymbol{k}|}\int\rho V_{ij}(y_2,\boldsymbol{k},\omega)e^{-|\boldsymbol{k}|y_2}dy_2 + \frac{ik_\alpha}{|\boldsymbol{k}|}\hat{\sigma}_{\alpha 2}(\boldsymbol{k},\omega) \tag{49}$$

where $\hat{\sigma}_{\alpha 2}(k,\omega)$ is the Fourier transform of the wall shear stresses at $y_2=0$. Eq. (49) indicates that including viscous shear stresses could lead to a non zero spectrum at zero wavenumber. Although not free from controversy (Howe, 1992; Dowling, 1998), the estimated non zero shear stress near zero wavenumber by Kronauer, Hollis, Bullock, and Lai (1997) may substantiate this assumption.

Chase (1991) showed how the wall pressures and shear stresses can be related to the fluctuating Reynolds stresses, the main sources of fluctuating pressures. He assumed that $\hat{\sigma}_{\alpha 2}(k,\omega)$ need not vanish at zero wavenumber as do the wall pressures in inviscid flows. More specifically in the region, $\omega/c < k < 1/\delta$, the low wavenumber pressure amplitude is equal to that of the shear stress except they are 90° out of phase. A semi-empirical model for the wavevector-frequency spectrum of turbulent wall shear stress (which is equal to the low wavenumber pressure in amplitude) was constructed (Chase, 1993) based on the spectra of streamwise velocity in the sublayer of turbulent pipe flow measured by Morrison et al. (1971). This empirical shear stress spectrum at near zero wavenumber, $S(0,\omega)$, is shown below:

$$S(o,\omega)/(\rho^2 u_*^6 \omega^{-3}) = 0.00014\omega_+^{3/2}(1+3.5\omega_+)^{-4}[\omega_+/4+0.038+(0.0121a_+^2\omega_+)^{-1}]^{-3.5} \quad (50)$$

where $\omega_+ = \omega\nu/u_*^2$, $a_+ = \delta u_*/\nu$. Another set of near zero wavenumber spectra available in the literature was the pressure spectra published by Sevik (1986). As shown in Fig. 9, Sevik's data collapse quite well with Chase's empirical curve although Sevik's data (the underwater portion of the data) are only available in a rather small range of Strouhal numbers.

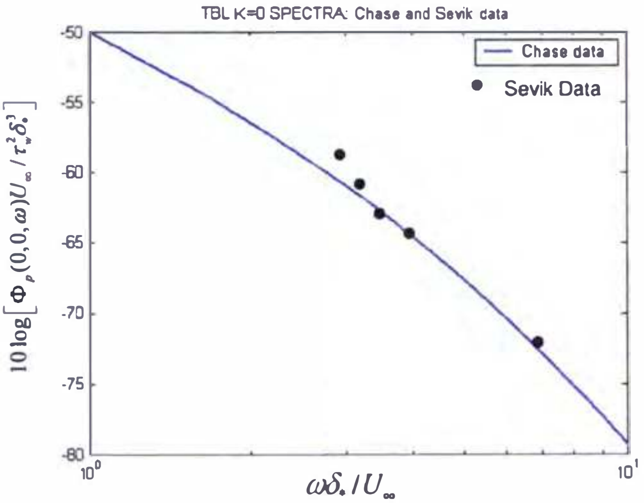

Figure 9. Chase's Empirical Zero Wavenumber Spectrum and Sevik's Data, the Normalized Spectrum in dB is $10\log\left[\Phi_p(0,0,\omega)U_\infty/\tau_w^2\delta_*^3\right]$

2.8 A Combined Chase Model

Chase's zero wavenumber spectrum discussed above may be assumed to be representative of the wavenumber independent spectrum in the low wavenumber region, which may be normalized by $\phi_p(\omega)(U_c/\omega)^2$ and then added to Eq. (31) to form the Combined Chase spectrum, i.e.,

$$f_{com.-chase}(\tilde{k}_1^2,\tilde{k}_3^2) = f_{chase87}(\tilde{k}_1^2,\tilde{k}_3^2) + f_S, \tag{51}$$

$$f_S = 0.00014\omega_+^{3/2}(1+3.5\omega_+)^{-4}[\omega_+/4+0.038+(0.0121a_+^2\omega_+)^{-1}]^{-3.5}\rho^2u_*^6\omega^{-3}(\omega/U_c)^2/\phi_p(\omega).$$

By so doing, one assumes that the spectra caused by shear stresses, f_S, are wavenumber independent in the low-wavenumber range, and a white pressure spectrum which equals f_S is added to the Chase's 1987 spectrum. Since the value of f_S is usually at least three orders of magnitude smaller than that of the convective ridge, the effect by adding f_S (in the low-wavenumber region) on the integrated sum of the normalized spectrum over the wavevector plane (to be unity) should be insignificant. From here on, this spectrum will be called the Combined Chase spectrum. Fig. 10 shows the comparison between Chase's 1987 and the Combined Chase spectrum at a small Strouhal number, say, $\omega\delta_*/U_\infty$=0.5. The two spectra show differences only in the low wavenumber region; the region where $(\tilde{k}_1^2+\tilde{k}_3^2)^{1/2}<0.1$. It is evident that by adding the low wavenumber white contents contributed by the shear stresses, the sharp dent at zero wavenumber of the Chase 1987 spectrum at low Strouhal number disappears. The Combined Chase spectrum is now smoother (with shallower dent). The white spectrum, however, is not realizable in the linear wavevector plane. The white spectrum can be seen only when it is broadened in logarithmic wavenumber scale. Fig. 11 shows the same comparison between the Corcos, Chase-1987, and the Combined Chase spectra as a function of k_1 observed at k_3=0. The Combined Chase spectrum now shows a low wavenumber white spectrum (the red curve) as it is plotted in the logarithmic wavenumber scale. This is for the case of low Strouhal number, $\omega\delta_*/U_\infty$=0.5, where adding the contribution by the viscous shear stresses significantly changes the low wavenumber spectrum.

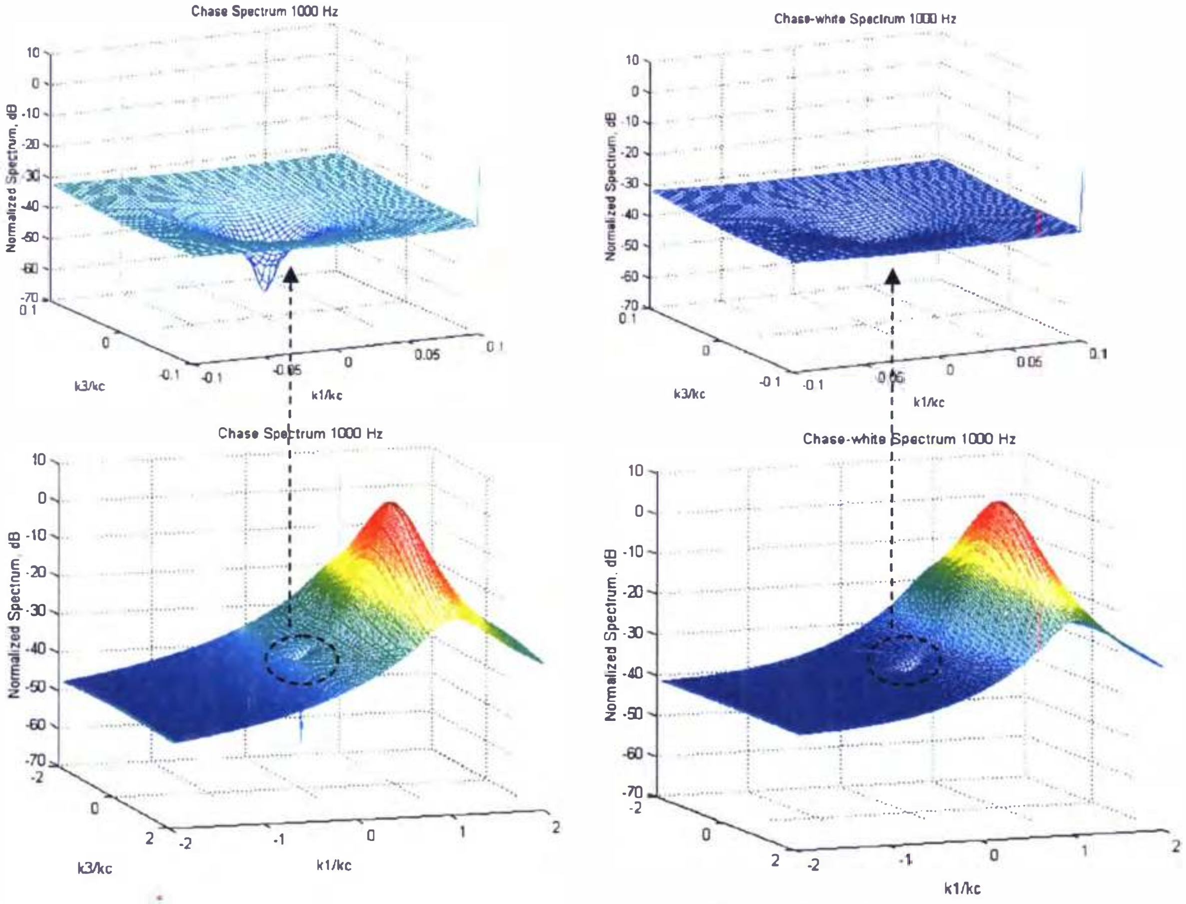

(a) Normalized Chase 1987 Spectrum

(b) Normalized Combined Chase Spectrum

Figure 10. Normalized Chase 1987 and Combined Chase spectra, $\omega\delta_* / U_\infty$=0.5

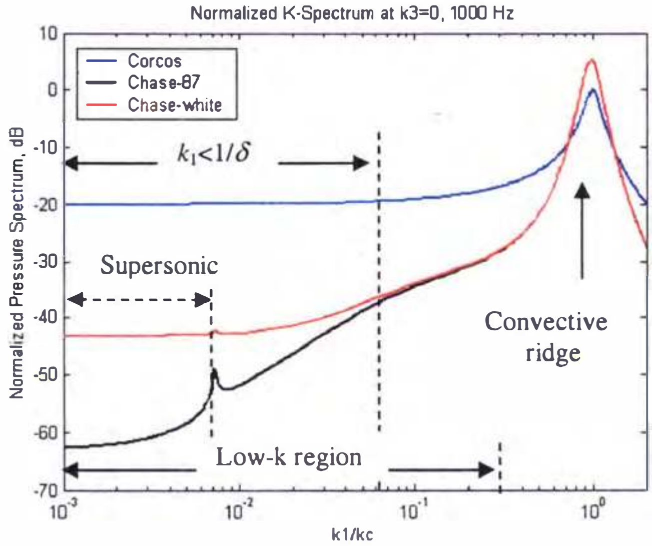

Figure 11. Normalized Corcos, Chase-87, and Combined Chase (Labeled here as Chase-White in Red) Spectra in Logarithmic Wavenumber Scale ($\omega\delta_* / U_\infty$=0.5)

Due to the more significant acoustic contributions at higher frequencies, the shear stress contributions are no longer significant at higher Strouhal numbers. This is shown in Fig. 12 (calculated with $U_\infty = 15 m/s$ and the length of the plate, L_p=5 *m*) where the Combined Chase and the Chase 1987 spectra are compared for various Strouhal numbers, ranging from 0.06 to 18. Shear stress contributions become less significant when Strouhal numbers are near or larger than 6 and become no effect at all when the Strouhal number is 18. This point may be further illustrated by Fig. 13, which shows the near zero wavenumber spectra as a function of $\omega\delta_* / U_\infty$ predicted from Chase-1987 acoustic and Chase-1993 shear stress models. Also shown in the figure is the Combined Chase near zero wavenumber spectrum which is the sum of the two spectra. The near zero wavenumber spectra, $\Phi_p(0,0,\omega)U_\infty / \tau_w^2\delta_*^3$, are expressed in the same way as that of Blake (1986), to provide a possible direct comparison with the other wind tunnel data. The low-wavenumber wind tunnel data shown are the least square fitted curves by Martin (1976) and Farabee-Geib (1976) and are acquired here from Blake (1986, Fig. 8-28). It is noted that the wind tunnel measurements were taken at the wavenumber region considerably deviated from near zero wavenumber region (see Fig. 14). The differences in the spectral levels in the two region shown in Fig. 14 may explain why the wind tunnel data shown in Fig. 13 are considerably higher than the near zero wavenumber spectra contributed by the wall shear stresses.

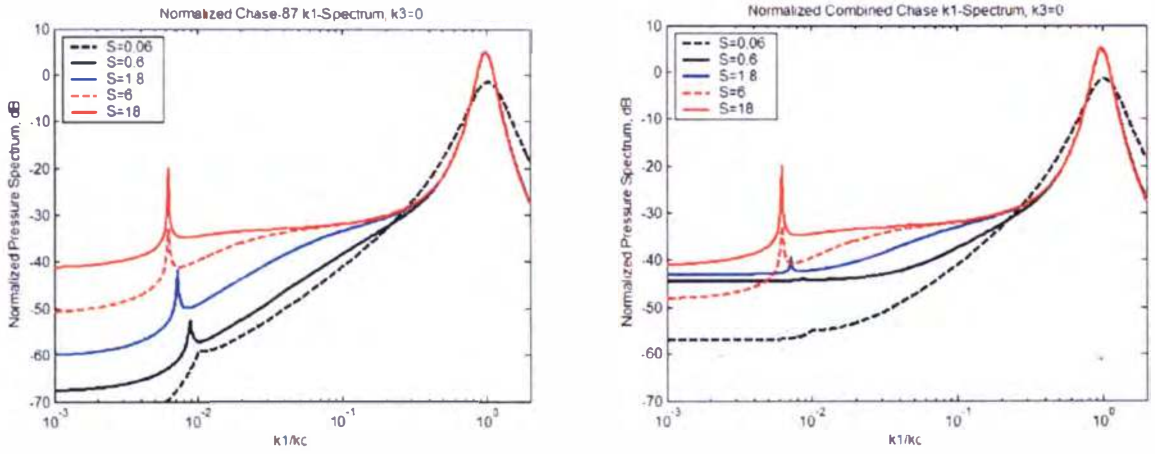

(a) Chase 1987 Spectrum

(b) Combined Chase Spectrum

Figure 12. Normalized Chase-87 and the Combined Chase spectra as a function of S= $\omega\delta_* / U_\infty$

It is shown in Fig. 13 that when the flow (underwater) conditions are, U_∞=15 *m/s* and δ=0.05 *m* (at 5 *m* from leading edge), the wall shear stress is the predominant contributor of the near zero wavenumber spectra when $\omega\delta_* / U_\infty$ <10, and when $\omega\delta_* / U_\infty$ >10, Chase's suggested acoustic contribution will be the dominant contributor. It also shows that at a different flow condition, where U_∞=10 *m/s* and δ=0.02 *m* (at 1 *m* from leading edge), the change of the predominant contributor occurs when $\omega\delta_* / U_\infty$ =7.5 instead of $\omega\delta_* / U_\infty$ =10 in the previous case. Unlike Corcos's spectrum where one normalized spectrum, Eq. (23), is universally applied to all frequencies, both the normalized Chase 1987 and the Combined Chase spectra are speed and frequency dependent.

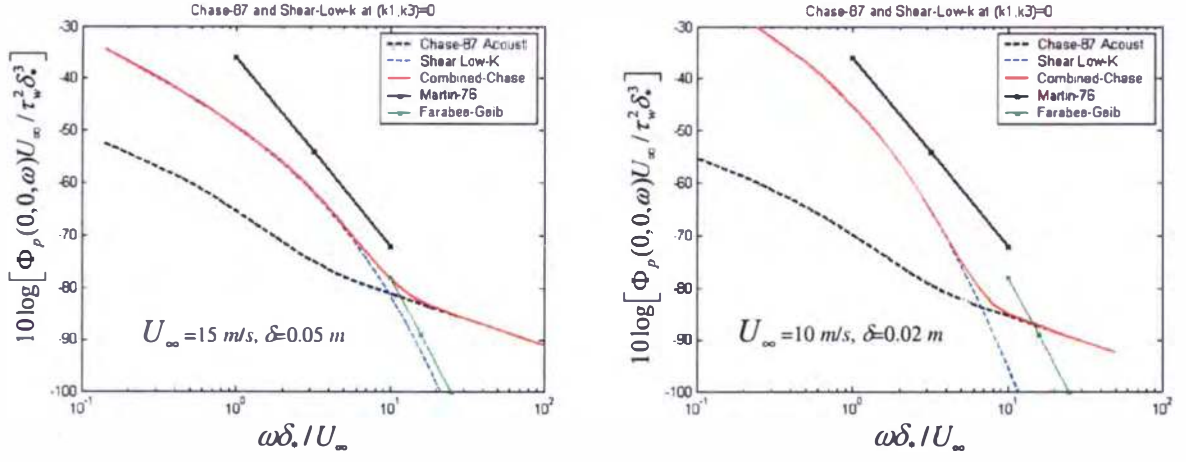

Fig. 13 Near zero wavenumber spectra predicted from Chase-1987 acoustic, Chase-1993 shear stress, and Combined Chase models and the Low-wavenumber Wind Tunnel Data by Martin and Farabee-Geib

2.9 Comparison of the Various Spectral Models

Fig. 14 shows the comparison of the normalized k_1-spectra computed from the models of Corcos (1963), Witting (1986), Smol'yakov-Tkachenko (1991), Modified Corcos, Chase (1987) and the current Combined Chase. It shows that the Witting-86, Modified Corcos, Chase-87 and the Combined Chase spectra are clustered together within a couple of dB for k_1>0.1 k_c at $\omega\delta_*/U_\infty=1$ and for the nearly entire subsonic range when $\omega\delta_*/U_\infty=10$. Noting that Chase-87 spectrum is empirically fitted with data in these ranges, this may be reason why the Modified Corcos spectrum has been used successfully by many investigators such as Ko and Schloemer (1991), Hambric and Hwang (2000) and others. However, the Modified Corcos as well as the Witting spectra are considerably higher in level than both the Chase-87 and the Combined Chase spectra in the supersonic region and at low subsonic wavenumbers as well when Strouhal numbers are low. Although Witting-86 and the Modified Corcos spectra collapse nicely within a couple of dB at all wavenumbers except near the convective ridge, they cannot justifiably be used in the supersonic and low subsonic wavenumbers regions. At the convective ridge, the Witting spectrum is unusually sharp and high (see Figs. 5 and 14) and may cause errors when the contributions to the excitation are dominated by the convective ridge. As mentioned earlier, the Corcos-63 spectrum is about 20 dB too high at low wavenumbers. Although the Smol'yakov and Tkachenko spectrum may be nearly correct in the supersonic range, at nearly all subconvective wavenumbers it falls about 15 dB too low.

At this point, the Combined Chase spectrum is the most empirically justifiable model. Unfortunately, it is not possible to obtain a corresponding cross-spectral density function in a closed form solution, as noted by Chase (1987), via inverse Fourier transformation. Despite the simplicity in the mathematical descriptions for both the cross-spectral density function and the wavevector-frequency spectrum, the Modified Corcos spectrum agrees remarkably well with the Combined Chase spectra, except in the supersonic region and at low subsonic wavenumbers when Strouhal numbers are low. The possible impact of this deficiency will be evalued in Section 3. Although Witting also agrees well with the Combined Chase spectrum, Witting spectrum does not have a simple descriptive form [see Eq. (35)], and does have the corresponding cross-spectrum necessary for use with numerical models. For subsonic low wavenumber excitations in finite-element models of structures, it may be plausible to use the Modified Corcos cross-spectrum to approximately represent the cross-spectrum for the Combined Chase wavevector-frequency spectrum.

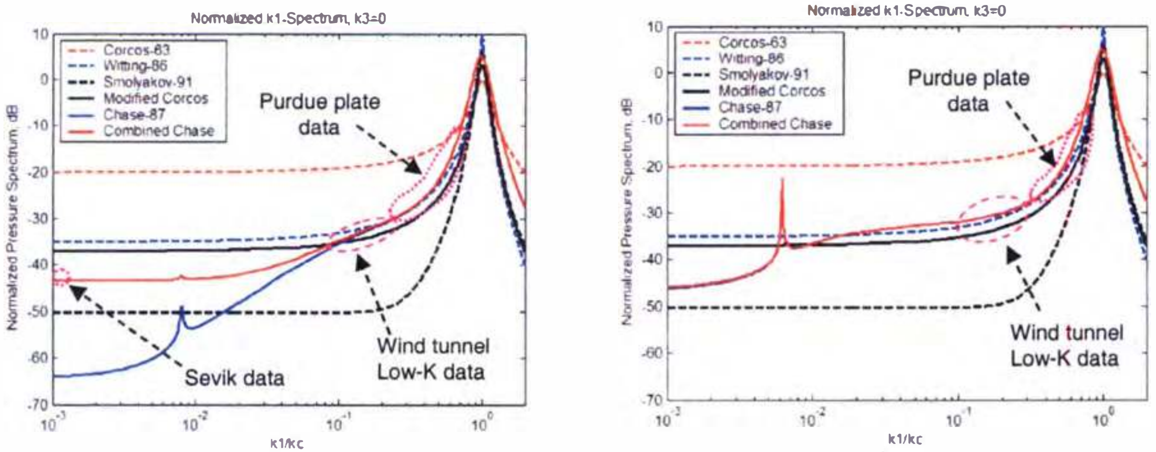

$\omega\delta_* / U_\infty = 1$ $\omega\delta_* / U_\infty = 10$

Figure 14. Comparison of the Various Models at Two Strouhal Numbers

As indicated in Figure 14, three regions of wavenumbers exist where data are available for comparing with the spectral models. Near the zero wavenumber region, Sevik's data agrees with Chase's wall shear stress caused pressure, which is the dominant contributor of the Combined Chase spectrum when $\omega\delta_* / U_\infty < 10$. However, the Combined Chase near zero wavenumber spectrum in the neighborhood of $\omega\delta_* / U_\infty = 10$ or larger will be predominantly contributed by the acoustic components (see Fig. 13). Therefore, there is no experimental data to support the Combined Chase spectrum when $\omega\delta_* / U_\infty > 10$. In a subconvective range, where $0.1 < k_1 / k_c < 0.25$, is the region where most low wavenumber spectra were measured (e.g., Martin and Leehey, 1977; Farabee and Geib, 1976). The Combined Chase, Modified Corcos and Witting spectra agreed well with data in this region. In the higher wavenumber subconvective range, where $0.3 < k_1 / k_c < 0.75$, the Modified Corcos spectrum is confirmed (so are the Combined Chase and Witting spectra since they collapse) by an analysis by Hambric and Hwang (2000) using the experimental data obtained from a Purdue University wind tunnel by Han, Bernhard, and Mongeau (1999). However, in the crucial wavenumber region of underwater interest where $0 < k_1 / k_c < 0.1$, there is no experimental data available to confirm any of the models.

It is noted that the normalized empirical low wavenumber spectra such as the Chase's supersonic, near zero wavenumber shear stress spectra, and the zero wavenumber Sevik data,

$f(\tilde{k}_1 \approx 0, \tilde{k}_3 \approx 0)$, discussed above have been normalized using the Chase's point frequency spectrum shown in Eq. (30). In order to recover the actual values of these wavenumber-frequency spectra, Eq. (30) must be used. On the other hand, both the normalized spectra, $f(\tilde{k}_1, \tilde{k}_3)$, of the Corcos and the Modified Corcos models are independent of what value of the point frequency spectra are used to normalize them (see Eqs. 23 and 44). Since the normalized wavenumber spectra are merely showing the relative distribution in wavenumbers of the point frequency spectrum, which sum over the normalized wavevector plane ($\tilde{k}_1, \tilde{k}_3$) is always unity. We, therefore, assume that all of the normalized wavenumber spectra established above can be applied in the same way as those of the Corcos and the Modified Corcos models, i.e., $\Phi_p(\boldsymbol{k},\omega) = \phi_p(\omega)(U_c/\omega)^2 f(\tilde{k}_1, \tilde{k}_3)$, where the value of $\phi_p(\omega)$ can be determined by an independent experiment or calculated from a predictive model.

3.0 Point Frequency Spectrum

The frequency density function of the wall pressure depends strongly on the flow parameters. Its value is usually determined according to experimental curves plotted according to certain scaling laws (Blake, 1986; Farabee and Casarella, 1991; Keith, Hurdis, and Abraham, 1992; Goody, 2002). For example, the low frequency spectrum scales well with outer variables such as the boundary layer thickness, while the high frequency spectrum scales better with inner variables such as the wall shear stresses. All scaling parameters depend on the Reynolds number (in terms of distance from the leading edge, boundary layer thickness, or momentum thickness) of the flow. It is quite cumbersome to determine the point-to-point variations of the pressure spectra on the surface of a vehicle using the non-dimensional curves. In the past (Chase,1980; Ko and Schloemer, 1989), the following simple approximation had been used,

$$\phi_p(\omega) = a_0 \rho_o^2 v_*^4 \omega^{-1}, \quad \text{for } \omega\delta_*/U_\infty > 0.5, \tag{52}$$

where a_0 is a proportionality constant which may vary from 1 to 5. This formula, however, provides a satisfactory approximation only when the Strouhal number (in terms of displacement thickness) falls approximately between ½ and 5. Two frequency spectral models have been discussed: one is Chase's model shown in Eq. (30) and the other is Witting's model shown in Eq. (34).

In an investigation of the vibration response of spacecraft shrouds to in-flight fluctuating pressures, Cockburn and Robertson (1974) utilized the following semi-empirical equation for the frequency spectrum of wall pressures beneath a homogeneous and attached boundary layer at transonic and supersonic speeds:

$$\phi_p(\omega) = \frac{1}{4\pi}\left(\frac{q_\infty^2 \delta}{U_\infty}\right)\left(\frac{\overline{P^2}/q_\infty^2}{(\delta f_o/U_\infty)[1+(\omega/2\pi f_o)^{0.9}]^2}\right) = \frac{1}{4\pi}\left(\frac{\overline{P^2}}{f_o[1+(\omega/2\pi f_o)^{0.9}]^2}\right), \tag{53}$$

where q_∞ is the local free stream dynamic pressure, $\overline{P^2} \approx [0.006/(1+0.14M^2)q_\infty]^2$ is the mean square fluctuating pressure, M is the local Mach number, and f_0 is the characteristic frequency: $f_o = 0.346U_\infty/\delta$. The Cockburn and Robertson frequency spectrum represents the frequency distribution of the mean square pressure as a function of the characteristic frequency, which is characterized by only the outer variables, U_∞ and δ.

Smol'yakov and Tkachenko (1991) also provided their empirical frequency spectrum expressed in terms of both inner and outer variables:

$$\phi_p(\omega) = 5.1\tau_w^2\delta_*/[U_\infty(1+0.44(\omega\delta_*/U_\infty)^{7/3})] \tag{54}$$

where, in the case on a flat plate, the wall shear stress and boundary thickness can calculated approximately by $\tau_w = 0.029\rho U_\infty^2\left(\frac{\nu}{U_\infty L}\right)^{1/5}$, $\delta = 0.37L\left(\frac{\nu}{U_\infty L}\right)^{1/5}$, L is the linear length from the leading edge, and in water, $\delta_* \approx \delta/8$.

Recently, Smol'yakov (2000), developed a simple method for calculating the TBL wall pressure spectra based on the source mechanisms that generate wavenumber spectrum caused by the interactions between turbulence and the mean shear, i.e.,

$$P_s(k_1,k_3,\omega) = \rho\frac{k_1}{|k|}\int_0^\infty\frac{\partial U}{\partial y}V_2(k_1,y,k_3,\omega)e^{-|k|y}dy \tag{55}$$

This is a special case of Eq (29), since here the spatial Fourier transform is only applied to the velocity fluctuation normal to the wall in the plane *y*=constant. *U* is the average velocity in the boundary layer at a distance *y* from the wall. From this, the wavenumber-frequency transform of the wall pressure is consequently,

$$\Phi_p(k_1,k_3,\omega) \approx \frac{k_1^2}{|k|^2}\int_0^\infty\left(\frac{\partial U}{\partial y}\right)^2 G(k_1,k_3,\omega,y)e^{-2|k|y}dy \tag{56}$$

where $G(k_1,k_3,\omega,y) = f(y)(k_1^2+\beta^2k_3^2)\exp\{-\alpha\ell[|k|+|k_1|(\beta-1)]\}$ is a generalized wavenumber-frequency function of the pressure source function located at a distance *y* from the wall. This source function is therefore characterized by: (1) an asymmetry coefficient, $\beta\ (\approx 6.45)$; (2) a dimensionless coefficient, $\alpha\ (\approx 1/\pi)$, that determines the rate of decrease of the spectrum; (3) the eddy length scale, $\ell = \langle u_1u_2\rangle^{1/2}/(dU/dy)$, where $\langle u_1u_2\rangle$ is the correlation of the longitudinal and the transverse components of the turbulent velocity fluctuations at a distance *y* from the wall; and (4) a function of position, $f(y) \approx \kappa\ell^5$, where $\kappa \approx \langle u_1u_2\rangle^{1/2}$ is the characteristic value of the turbulent velocity fluctuations. For the mean shear term, two separate expressions are used in the inner and outer regions of the boundary layer. In the inner wall region (the constant stress region): $dU/dy = u_*^2/(\nu + \varepsilon)$, where ε is the eddy viscosity. In the outer region which occupies 85-87% of the boundary layer thickness: $dU/dy = (u_*^2/\varepsilon)\exp[-2.5(y/\delta)^2]$, where the eddy viscosity can be assumed to be a constant value.

With the generalized wavenumber-frequency source function and the mean shear terms given above, Smol'yakov computed the point frequency spectrum by evaluating the integral, from y=0 to $y \to \infty$, and over the entire wavevector plane, i.e.,

$$\phi_p(\omega) \approx \iint \frac{k_1^2}{|k|^2} \int_0^\infty \left(\frac{\partial U}{\partial y}\right)^2 f(y)(k_1^2 + \beta^2 k_3^2)\exp\{-\alpha\ell[|k| + |k_1|(\beta - 1)]\} e^{-2|k|y} dy dk_1 dk_3. \quad (57)$$

He also analyzed a diverse group of data reported in the literature with inner or outer variable scaling. As expected, outer variable scaled data collapse together at low frequencies but scattered at higher frequencies according to the increase of Reynolds number, $R_\theta (= U_\infty \theta / \nu)$, where θ is the momentum thickness. This observation was confirmed by his computed spectra. The inner variable scaled data are also collapsed at high frequencies, as expected. He further observed that in the intermediate frequencies, the peaks of the spectral curves are a smooth function of R_θ. Smol'yakov then argued for the requirement of different scaling for different frequencies and Reynolds numbers. Four distinctive characteristic frequency ranges, determined by dimensionless frequency, $\varpi = \omega\nu/u_*$, are distinguished for R_θ>1000:

$$\begin{aligned}
&\phi_p(\omega) = 1.49\times10^{-5} R_\theta^{2.74} \varpi^2 (1 - 0.117 R_\theta^{0.44} \varpi^{1/2})[u_*^2/(\tau_w^2 \nu)] \\
&\qquad \text{when } \varpi < \varpi_o \\
&\phi_p(\omega) = 2.75\varpi^{-1.11}\{1 - 0.82\exp[-0.51(\varpi/\varpi_o - 1)]\}[u_*^2/(\tau_w^2 \nu)] \qquad (58) \\
&\qquad \text{when } \varpi_o < \varpi < 0.2 \\
&\phi_p(\omega) = (38.9e^{-8.35\varpi} + 18.6e^{-3.58\varpi} + 0.31e^{-2.14\varpi})\{1 - 0.82\exp[-0.51(\varpi/\varpi_o - 1)]\}[u_*^2/(\tau_w^2 \nu)] \\
&\qquad \text{when } \varpi > 0.2
\end{aligned}$$

where the peak frequency occurs when $\varpi = \varpi_o = 49.35 R_\theta^{-0.88}$. In the low frequency region, $\varpi < \varpi_o$ and the pressure spectrum is proprtional to ω^2. In the mid frequency region, where ϖ is near ϖ_o, is the peak region. In the "universal" range, $\varpi_o < \varpi < 0.2$, and $\phi_p(\omega) \propto \omega^{-1}$. In this range, however, Smol'yakov's expression shows the spectrum to be proportional to $\omega^{-1.11}$ to account for the non perfect frozen pattern of the flow and the dependency of U_c on wavenumber. In the high frequency region, $\varpi > 0.2$, $\phi_p(\omega)$ varies from $\propto \omega^{-1.11}$ to $\propto \omega^{-5}$.

Most recently, Goody (2002) presents an empirical model based on the experimental surface pressure spectra measured by seven research groups. His empirical model is based on the ratio (R_T) of the outer boundary layer time scale (δ/U_∞) to the inner boundary layer time scale (ν / u_*^2). The effect of Reynolds number is incorporated through the time scale ratio. The final form of this empirical model is

$$\frac{\Phi(\omega)\, U_\infty}{\tau_w^2\, \delta} = \frac{3\left(\dfrac{\omega\delta}{U_\infty}\right)^2}{\left[\left(\dfrac{\omega\delta}{U_\infty}\right)^{0.75} + 0.5\right]^{3.7} + \left[C_3\left(\dfrac{\omega\delta}{U_\infty}\right)\right]^7} \tag{59}$$

where $C_3 = 1.1 R_T^{-0.57}$, $R_T = \left(\dfrac{u_* \delta}{\nu}\right)\sqrt{\dfrac{C_f}{2}}$, and where C_f is the friction coefficient.

This model compares well with experimental data over a large range of Reynolds numbers, $1400 < R_\theta < 23400$. Goody indicated that this model can be confidently extrapolated to higher Reynolds number of flows since the scaling behavior of the model strictly follows to the high frequency Reynolds number independent inner-layer scaling.

At this point, it is helpful to compare how the various frequency spectral models differ in the prediction of the wall pressure. In Fig. 15 (a), the point spectrum is predicted based on the following assumptions: $U_\infty = 21.34\, m/s$, L (from the leading edge)=0.45 m. This is the flow speed and one of the flush phone location in the Haddle and Skudrzyk (1969) experiments. The wall shear stress and boundary thickness are calculated approximately by the flat plate formula:

$\tau_w = 0.029 \rho U_\infty^2 \left(\dfrac{\nu}{U_\infty L}\right)^{1/5}$, $\delta = 0.37 L \left(\dfrac{\nu}{U_\infty L}\right)^{1/5}$, $\delta_* \approx \delta / 8$ and $\theta \approx 0.1\delta$.

In Fig. 15 (b), the point spectrum is predicted based on a slower speed, $U_\infty = 13\, m/s$, and a point much further down stream, L 9.45 m. Due to close proximity to the leading edge where the boundary layer is thinner, the peak frequency in Fig. 15(a) occurs approximately at 2 kHz while the chracteristic freuency, f_o , predicted from Cockburn-Robertson formulus is about 1 kHz. The highest frequencies shown in the figure are still within the "universal" range. Down stream where the boundary layer is thick, the peak frequency, as shown in Fig. 15(b), occurs below 100 Hz (f_o 48.5 Hz, from Cockburn-Robertson). Only the universal and higher frequency ranges defined by Smol'yakov are now displayed in the figure. The peak frequencies predicted by the Chase (Eq. 30), Witting (Eq. 34), and Smol'yakov (Eq. 58) formula are in good agreement. Goody's peak frequency occurs at slightly lower frequency. Both the Cockburn-Robertson (Eq. 53) and Smol'yakov-Tkachenko (Eq. 54) spectra, however, do not display spectral peaks near their corresponding characteristic frequencies. The Cockburn-Robertson spectrum was intended for vehicles at transonic and supersonic speeds and it may not be applicable for the lower speed ground or marine vehicles.

The spectra calculated using Chase, Goody and Smol'yakov expressions are within 5 dB of each other, exept at very low frequencies and at frequncies beyong the universal range, $\bar{\omega} > 0.2$. It is noted that the high frequency behavior of Chase's spectrum is such that $\phi_p(\omega) \propto \omega^{-1}$ as $\omega \to \infty$, which may not be accurate at frequencies beyond the universal range. The spectra calculated using Witting, Cockburn-Robertson and Smol'yakov-Tkachenko expressions deviate substantially from that calculated from Chase, Goody and Smol'yakov's expressions. A more thorough evaluation of the frequency spectral models will be given later in Section 4. As will be shown later, Smol'yakov (2000) and Goody (2002) models appear to be more accurate.

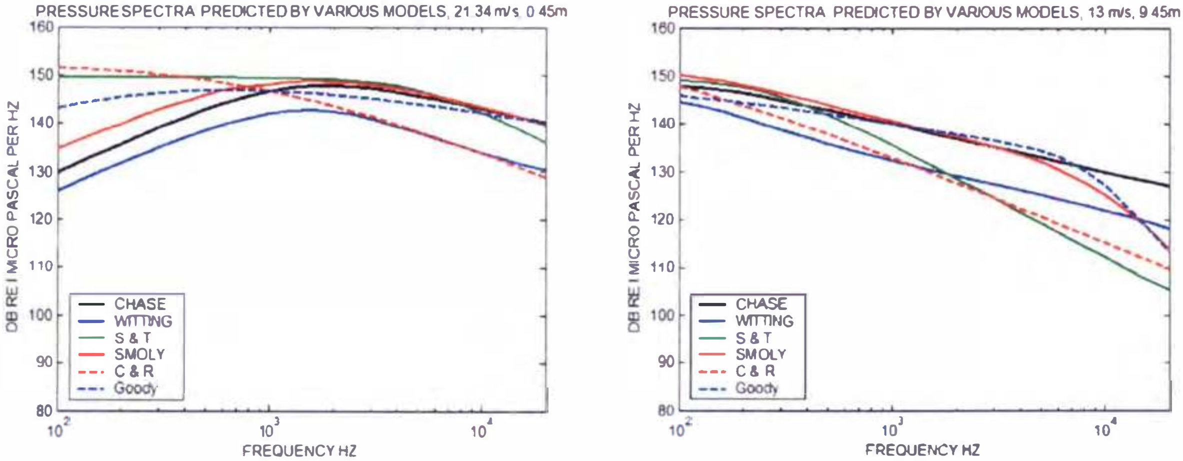

(a) $U_\infty = 21.34\, m/s;\, L = 0.45\, m$ (b) $U_\infty = 13\, m/s;\, L = 9.45\, m$

Figure 15. Wall Pressure Frequency Spectra Calculated from Chase (1987), Witting (1986), Smol'yakov and Tkachenko (1991, labeled S & T), Smol'yakov (2000), Goody (2002) and Cockburn-Robertson (1974, labeled C & R) Models

4.0 EXPERIMENTAL VERIFICATION OF THE MODELS

A historical and theoretical overview has been given of the detailed features of various models of the turbulent boundary layer wall pressure wavevector-frequency spectra and the corresponding cross-spectral density functions. A model most suitable for underwater applications must be selected. However, the available measured underwater data are quite limited. Wall pressure spectral data exists from a 0.2 inch (5 mm) diameter hydrophone located 0.45 meter from the bow of a buoyancy test vehicle (BTV) at 21.34 m/s flow speed (Abarbanel, Katz, and Cembrola, 1994). Further down stream, about 9.45 meter from the bow, wall pressure data exists from a 1/10 inch (2.54 mm) diameter hydrophone mounted on a large scale buoyancy test model at 13 m/s flow speed. These data provide an opportunity to assess the current capability of predicting the wall pressure frequency spectra at very thin (the former) and very thick (the latter) boundary layer thicknesses. The latter set of data was obtained from a flush mounted sensor designed to monitor the TBL characteristics in a conformal array experiment reported by Sherman, Ko, and Buehler (1990).

Validating the wavevector-frequency spectrum requires measurements by larger hydrophones, arrays of hydrophone, or flow-induced vibrations of underwater structures. The array data reported by Sherman, Ko, and Buehler (1990) are limited only up to a few hundred Hz, not high enough for useful verification. Flow noise measurements by Haddle and Skudrzyk (1969) used various shapes of hydrophone with diameters up to two inches mounted on the surface of a metal buoyant unit (19 inch diameter, 12 feet 5 inch long, ¼ inch thick aluminum shell). Pressure sensors were mounted at two locations: 17 inch from and bow, and 142 inch from the bow. This provides a broad range of boundary layer thickness and Strouhal number due to the wide range of frequencies reported (160 Hz to 40 kHz). The 1-inch diameter hydrophone data are the most consistent with the expected dependency in frequency and boundary layer thickness (or Strouhal number).

The wall pressure spectrum measured by a finite size circular pressure sensor, $\phi_M(\omega)$, with uniform pressure sensitivity can be calculated when the wavevector-frequency spectrum and the wavenumber response function, $H(k_1,k_3)$, are given (Ffowcs Williams, 1982; Capone and Lauchle, 1995):

$$\phi_M(\omega)=\int_{-\infty}^{\infty}\int_{-\infty}^{\infty}\Phi_p(k_1,k_3,\omega)H(k_1,k_3)dk_1dk_3 \qquad (60)$$

where $H(k_1,k_3)=\left[2J_1(\sqrt{k_1^2+k_3^2}a)/\sqrt{k_1^2+k_3^2}a\right]^2$, and a is the radius of the pressure sensor. The wavenumber response function, $H(k_1,k_3)$, has uniform wavenumber sensitivity when the diameter is near zero. When the sensor diameter is large, it becomes essentially a low-pass wavenumber filter. Fig. 16 shows the calculated $H(k_1,0)$ for 1/10-inch and 1-inch circular transducers at 100 Hz, 1000 Hz and 10,000 Hz, plotted as a function of k_1/k_c assuming U_∞=15 m/s. It is shown that in a 1-inch diameter sensor, the convective ridge excitations will be effectively filtered out. Fig. 17 shows the product, $\Phi_p(k_1,0,\omega)H(k_1,0)$, where the integrated sum will be the sensor measured frequency spectral density. It is also shown that at 10 kHz, the per wavenumber contributions by the convective ridge to the 1 inch phone pressure are about 15 dB lower than that contributed by the low wavenumber region, indicating a significant low wavenumber contributions at high frequencies for a large sensor. At very low frequency, e.g., 100 Hz, there is no filtering effect for both 1/10-inch and 1-inch sensor.

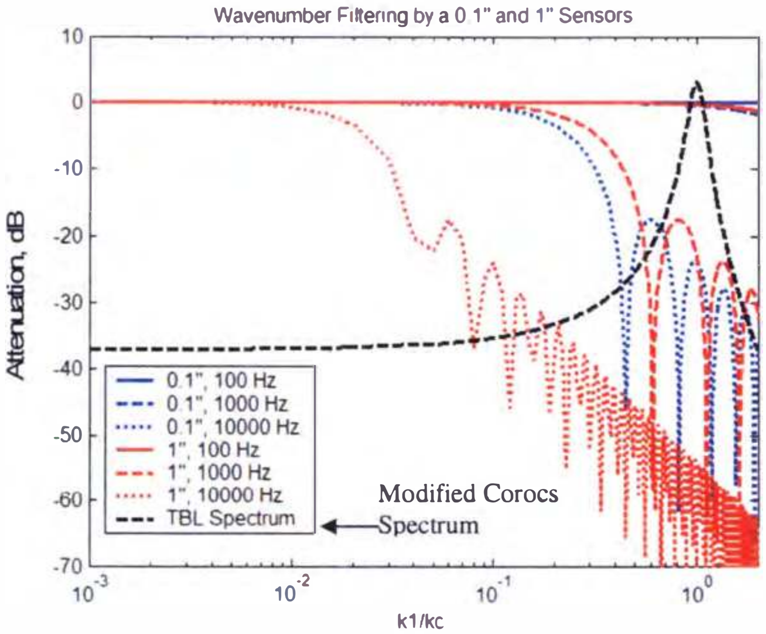

Figure 16. Wavenumber Filtering Effects of 1/10-inch and 1-inch Circular Transducers at 100 Hz, 1000 Hz and 10,000 Hz (U_∞=15 m/s), where Attenuation in db is Equal to 10log ($H(k_1,0)$)

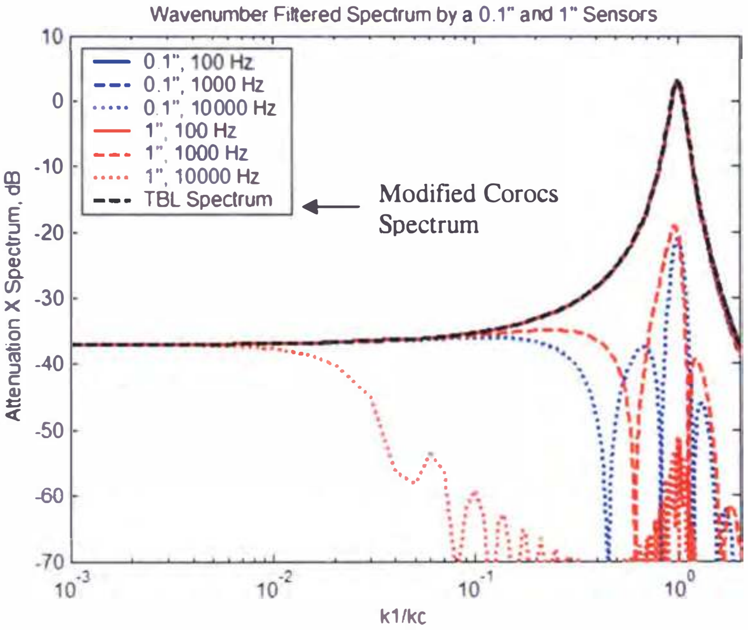

Figure 17. Filtered Spectral Contributions, $\Phi_p(k_1,0,\omega)H(k_1,0)$, to the 1/10-inch and 1-inch circular Transducers at 100 Hz, 1000 Hz and 10,000 Hz (U_∞=15 m/s)

According to Eqs. (22) and (60), The ratio of the measured pressure by a finite sensor and the point pressure, $\phi_M(\omega)/\phi_p(\omega)$, can be calculated as follows:

$$\phi_M(\omega)/\phi_p(\omega) = \int_{-\infty}^{\infty}\int_{-\infty}^{\infty} f(\bar{k}_1, \bar{k}_3) H(k_1, k_3) dk_1 dk_2 \tag{61}$$

where $f(\bar{k}_1, \bar{k}_3)$ is the normalized dimensionless spectrum, and $\phi_M(\omega)/\phi_p(\omega)$ is the so called Corcos attenuation factor. The point frequency $\phi_p(\omega)$ is contributed by all wavenumbers without attenuation. Due the increase of attenuation at a given wavenumber increases with frequency, the major contributions to $\phi_M(\omega)$ will be shifted to lower wavenumbers as frequency is increased. Using Eq. (60), the contributions to $\phi_M(\omega)/\phi_p(\omega)$ by three sub-regions: (1) the wavenumber spectrum in the acoustic domain where $|k| \le \omega/c$, (2) the low wavenumber region where $\omega/c < |k_1| < k_c/4, -\infty < |k_3| < \infty$, (3) the subconvective and ridge regions where $\omega/c < |k_1| < k_c/4, -\infty < |k_3| < \infty$, and the entire wavenumber range, where $-\infty < |k_1| < \infty$, $-\infty < |k_3| < \infty$ are computed.

Fig. (18a) compares the overall $\phi_M(\omega)/\phi_p(\omega)$ calculated from the Corcos, Modified Corcos, and the Combined Chase spectra for the one-inch diameter circular phone located 17 inches from the bow with a flow speed of 21.6 m/s. Figs. (18b), (18c) and (18d), on the other hand, show the relative contributions by the three regions calculated from the Corcos, Modified Corcos, and the Combined Chase spectra, respectively. This shows that due to the much higher low wavenumber spectrum, the value $\phi_M(\omega)/\phi_p(\omega)$ predicted by the Corcos spectrum is much higher than that predicted by the Modified Corcos and the Combined Chase spectra. As it is shown in Fig. 18b, the low wavenumber region becomes dominant source above 2 kHz when the Corcos spectrum is used. However, when the Modified Corcos and the Combined Chase spectra are used, the excitations are still dominated by the convective ridge region up to approximately 5,000 Hz. Above 5,000 Hz, the low wavenumber region is then the predominant source, and above 10 kHz, both the low wavenumber and acoustic regions are equal likely the predominant source. There is no noticeable differences in the values of $\phi_M(\omega)/\phi_p(\omega)$ predicted by the Modified Corcos and the Combined Chase spectra. The reasons for this are: (1) At low and mid frequencies, the excitation is dominated by the convective ridge and the subconvective region (the higher wavenumber portion of the low wavenumber region), where there is little difference between the two spectra. The differences occur at lower wavenumbers (including the acoustic regions) which are not the dominant source at low and mid frequencies, (2) At higher frequencies, the Combined Chase non acoustic low wavenumber spectra are close to that of the Modified Corcos spectra (see Fig. 14), and (3) In the entire frequency range shown, the acoustic region has no dominant influence in the excitation due the limitation of the sensor area. The differences may only be realizable when predictions are made for a large array of sensors or a large structure.

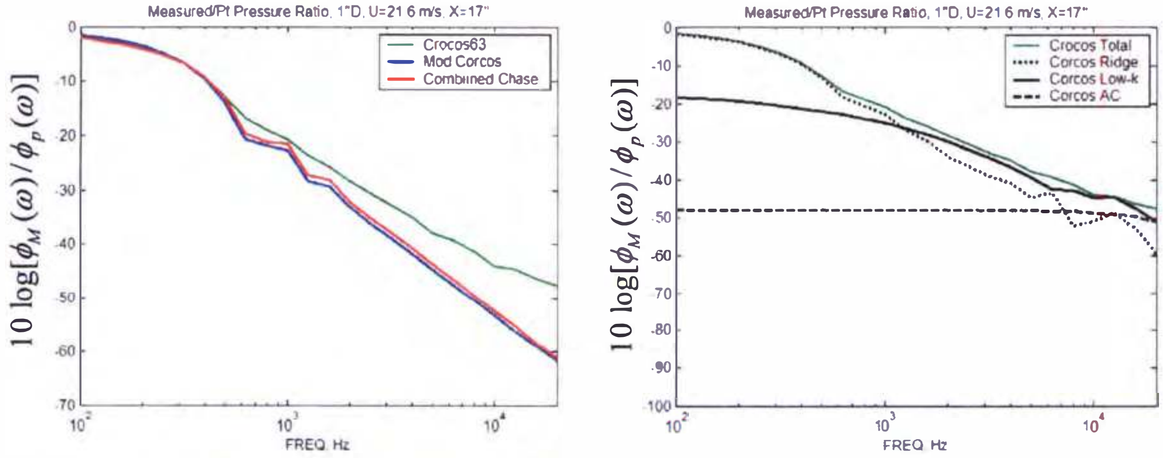

(a) $\phi_M(\omega)/\phi_p(\omega)$ by all wavenumbers

(c) $\phi_M(\omega)/\phi_p(\omega)$ by 3 regions of k

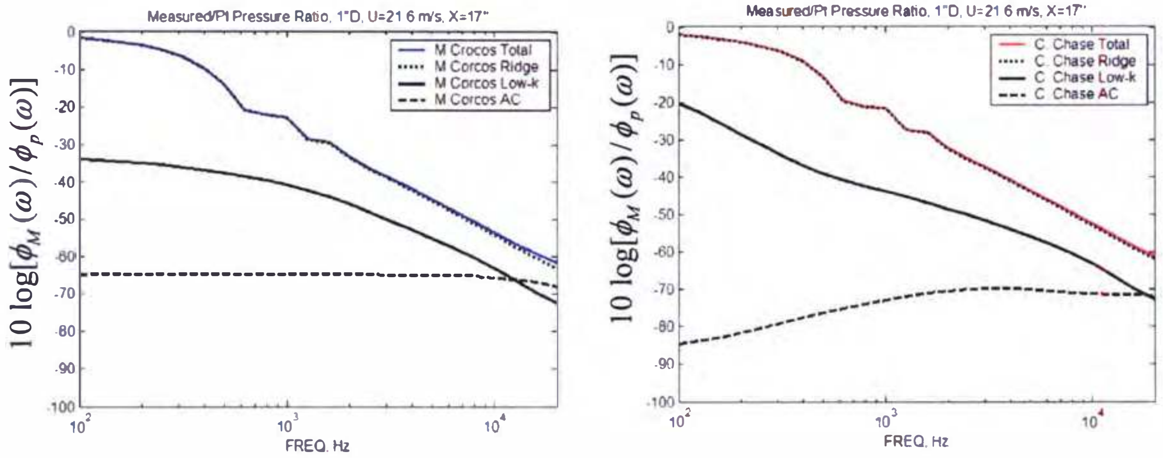

(b) $\phi_M(\omega)/\phi_p(\omega)$ by 3 regions of k

(d) $\phi_M(\omega)/\phi_p(\omega)$ by 3 regions of k

Figure 18. Comparison of $\phi_M(\omega)/\phi_p(\omega)$ Calculated from the Corcos, Modified Corcos, and the Combined Chase Spectra.

Calculations of the ratio between the hydrophone measured pressure and the theoretical point pressure, $\gamma(\omega)\,[=\phi_M(\omega)/\phi_p(\omega)]$ for the various models of $f(\tilde{k}_1, \tilde{k}_3)$ have been discussed above. This ratio is independent of which point spectral model is used. The calculated pressure spectrum measured by a finite size sensor is obviously

$$\phi_M(\omega) = \gamma(\omega)\phi_p(\omega) \qquad (62)$$

which will then depend on which point frequency, $\phi_p(\omega)$, spectral model in used. For the purpose of comparing the performance of the various point frequency spectral models, the Modified Corcos spectrum is used for calculating $\gamma(\omega)$ due to its simplicity. The other reason is because there is no difference between using the Combined Chase or the Modified Corcos spectra for hydrophones up to 1 inch in diameter. Figs. 19 and 20 show the calculated results using four different point frequency spectral models (Chase, Goody, Smol'yakov-Tkachenko, and Smol'yakov models). Predicted values are shown in solid lines while the corresponding data are shown in dotted lines. The Smol'yakov-Tkachenko model results are labeled "S & T". Fig. 19 shows the results for two upstream sensors: one is the 0.2 inch BTV senor located at 0.45 meter from the bow at 21.3 m/s flow speed, the other is the 1 inch Haddle and Skudrzyk sensor located at 0.43 meter from the bow at 21.6 m/s flow speed. Predicted trends by all models are consistent with the data. However, the most recently published models by Smol'yakov (2000) and Goody provide a slightly better overall agreement with data. Fig. 20 shows the results for two downstream sensors: one is the 0.1 inch senor located at 9.45 meter from the bow of a large scale buoyant unit at 13 m/s flow speed, the other is the 1 inch Haddle and Skudrzyk sensor located at 3.6 meter from the bow at 21.6 m/s flow speed. Predicted trends by all models are also consistent with the data. Again, the most recently published models by Smol'yakov (2000) and Goody (2002) provide the better overall agreement with data.

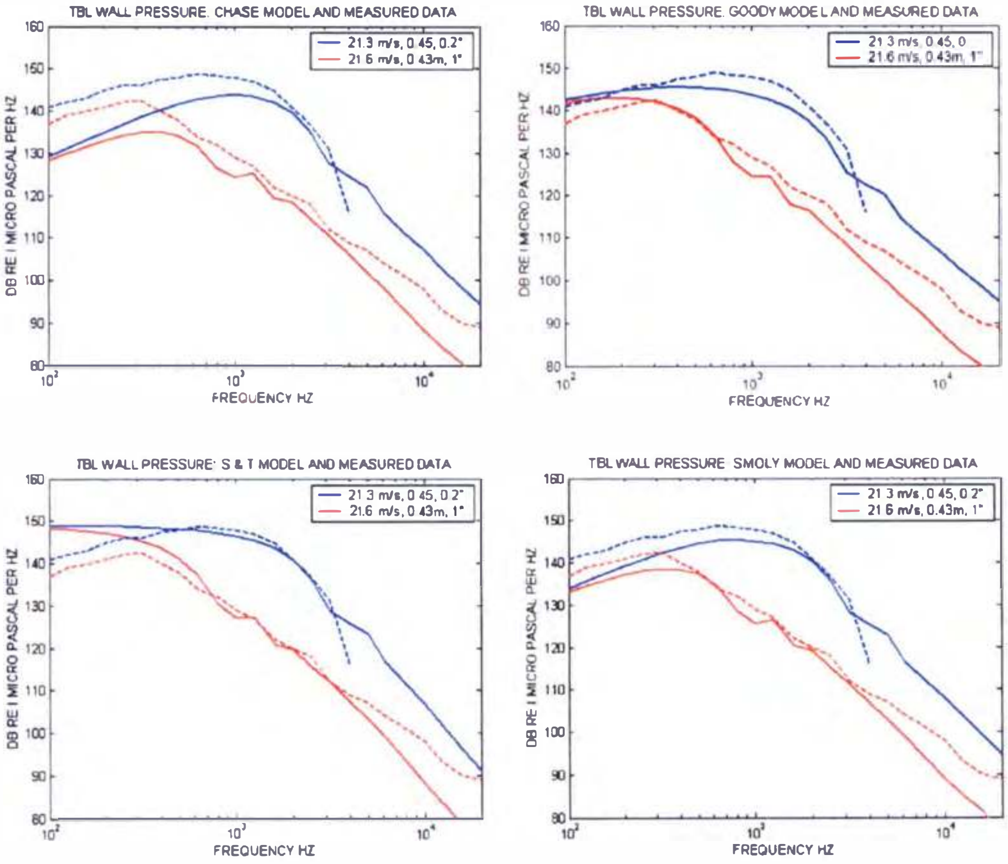

Figure 19. Predicted and Measured results for the 0.2 inch BTV senor located at 0.45 meter from the bow at 21.3 m/s flow speed and the 1 inch Haddle and Skudrzyk sensor located at 0.43 meter from the bow at 21.6 m/s flow speed.

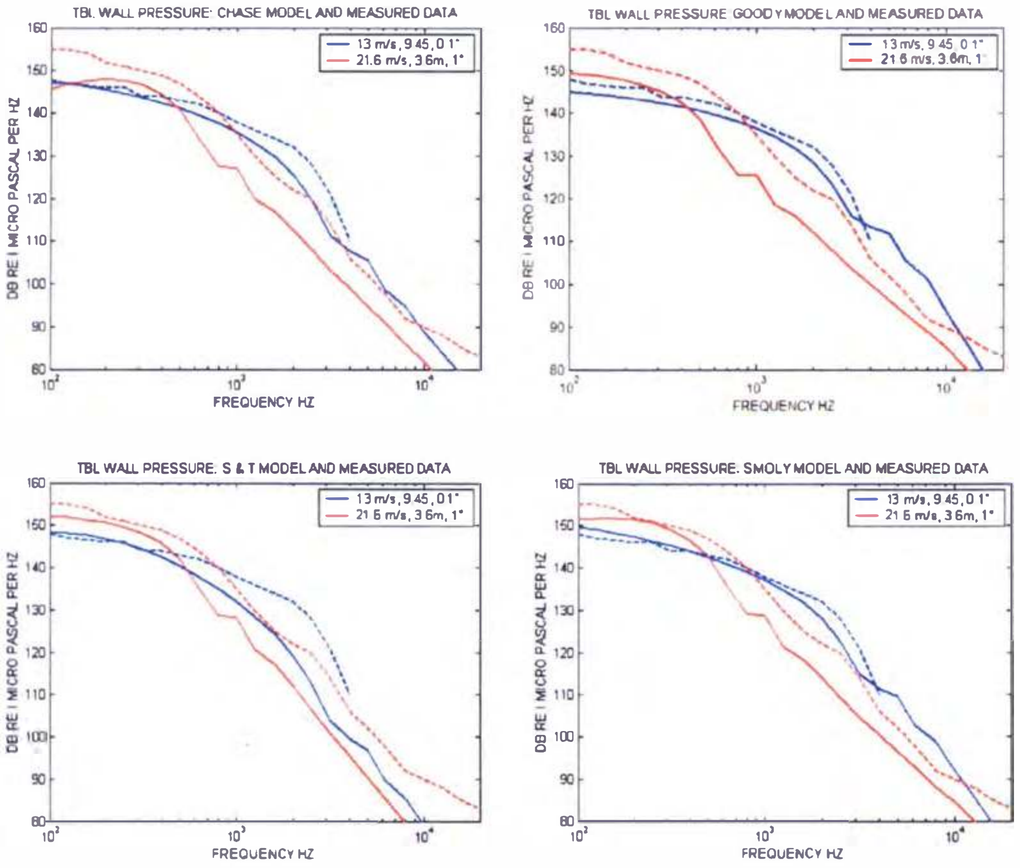

Figure 20. Predicted and Measured Results for the 0.1 inch Senor Located at 9.45 Meter from the Bow in a Large Scale Buoyant Unit at 21.3 m/s Flow Speed and the 1 inch Haddle and Skudrzyk Sensor Located at 3.6 Meter from the Bow at 21.6 m/s Flow Speed.

Predicted values are generally lower than that measured at larger Strouhal numbers. In the upstream sensors, predicted values become lower beginning around 4000 Hz while the down stream sensors beginning around 400 Hz. It is suspected that hull vibrations may contribute to the measured pressure by the hull mounted sensors. Based on plate theory, the spatial mean velocity response of an infinite plate $\phi_v(\omega)$ can be determined if the wavevector-frequency spectrum is given, i.e.,

$$\phi_v(\omega) \approx \frac{\pi^2 \omega^2}{2D^2 k_p^6 \eta} \Phi_p(k_1, k_3 \omega), \quad \sqrt{k_1^2 + k_3^2} = k_p \qquad (63)$$

where k_p is the plate bending wavenumber, and $D = Eh^2/[12(1-\nu^2)\rho_s]$. The vibration induced pressure spectrum, $\phi_{p,v}(\omega)$ is then approximately,

$$\phi_{p,v}(\omega) \approx \frac{\pi^2\omega^4\rho^2}{2D^2k_p^8\eta}\Phi_p(k_1,k_3\omega). \qquad (64)$$

When the vibration induced pressure is added, the ratio between the measured pressure by a finite sensor and the point pressure, $\phi_M(\omega)/\phi_p(\omega)$, is then calculated as follows:

$$\phi_M(\omega)/\phi_p(\omega) = \int_{-\infty}^{\infty}\int_{-\infty}^{\infty} f(\tilde{k}_1,\tilde{k}_3)H(k_1,k_3)dk_1dk_2 + \phi_{p,v}(\omega)/\phi_p(\omega) \qquad (65)$$

Fig. 21 shows the results for the upstream (x=17" or 0.45 m) and downstream (x=142" or 3.6 m) sensors (both 1-inch diameter) in the Haddle-Skudrzyk experiments. The curves labeled, "HYDRODYNAMIC" are the predicted pressures contributed by TBL pressures; the curves labeled, "VIB-Chase87" and "VIB-Corcos" are the predicted $\phi_{p,v}(\omega)/\phi_p(\omega)$ values using the Chase-1987 and the Modified Corcos spectra, respectively. This analysis indicates that above 4 kHz the vibration induced noise may be significant in the Haddle-Skudrzyk experiments, and predicted noise will be closer to that measured when the vibration caused noise is included.

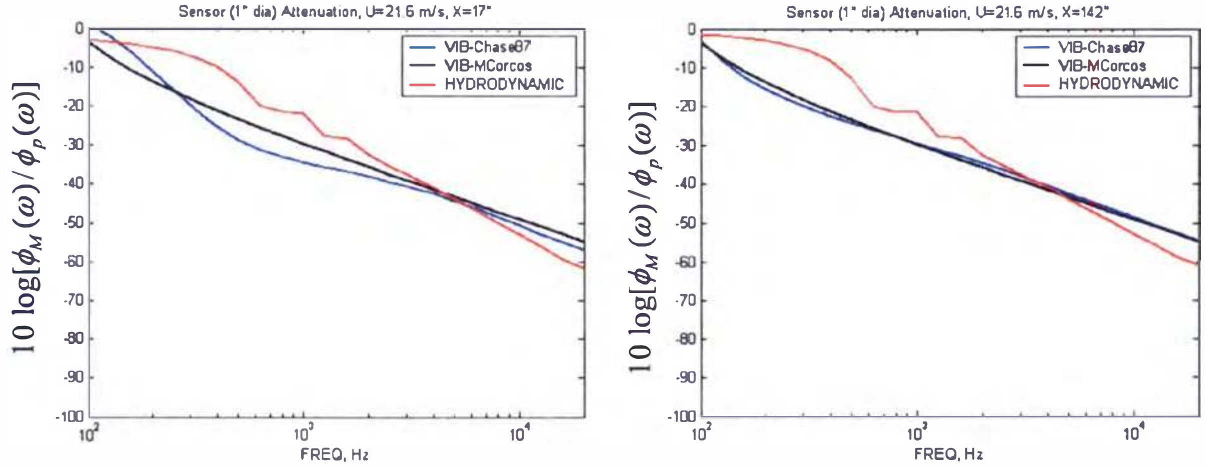

Figure 21. Predicted $\phi_M(\omega)/\phi_p(\omega)$ contributed by TBL Pressures and hull Vibrations

Figs. 22 shows the calculated results with the vibration induced pressures included for both the upstream and down stream sensors, using the normalized Modified Corcos wavevector spectrum and Smol'yakov's point frequency spectrum. Again, the upstream sensors are the 0.2 inch BTV senor located at 0.45 meter from the bow at 21.3 m/s flow speed and the 1 inch Haddle and Skudrzyk sensor located at 0.43 meter from the bow at 21.6 m/s flow speed; the downstream sensors are the 0.1 inch senor located at 9.45 meter from the bow of a large scale buoyant unit at 13 m/s flow speed, the other is the 1 inch Haddle and Skudrzyk sensor located at 3.6 meter from the bow at 21.6 m/s flow speed. Due to the predominant contributions by the convective pressures in the small sensors, such as the 0.1 inch and the 0.2 inch hydrophones, adding vibration caused pressures does not affect the predicted $\phi_M(\omega)$ at these sensors. However, with the vibration caused pressures included, the agreement between the predicted and measured values are much improved for the larger sensors, such as the 1 inch hydrophones.

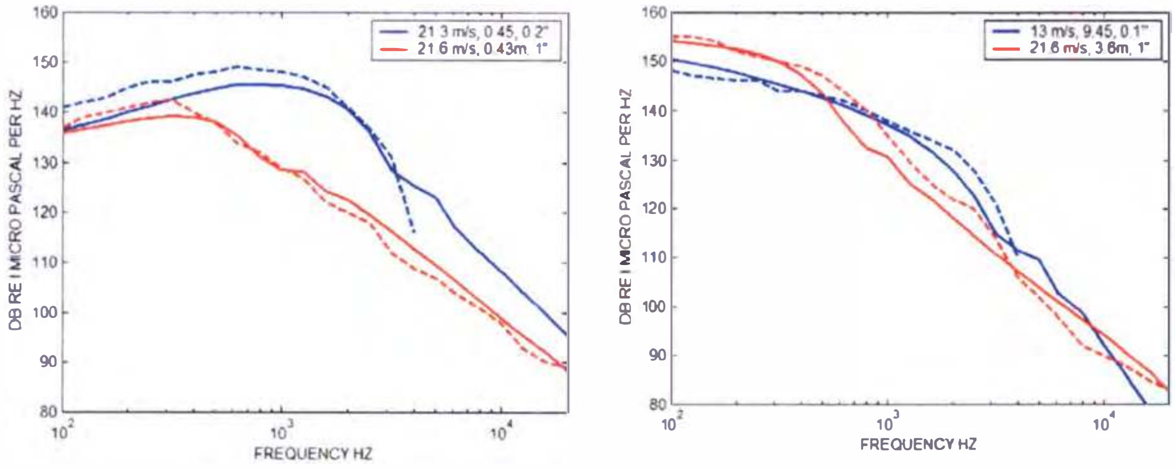

Figure 22. Predicted and Measured results for four Different Sensors at Different Locations of Buoyancy Propelled Vehicles when the Vibration Caused Pressures are Added

5.0 CONCLUDING REMARKS AND FUTURE WORK

A thorough examination of the theories, data, and empirical models of the wavevector-frequency spectrum as well as the cross-spectrum of the turbulent boundary layer wall pressures and shear stresses has been conducted for the purpose of seeking suitable structural forcing functions. The study indicates it is not possible to obtain a proper cross-spectral density function to serve as a structural loading function from experimental two-point correlation measurements. Determining the low wavenumber pressures must rely on the measured responses of a structural system or an array of pressure sensors subjected to TBL excitations. The cross-spectrum can be subsequently obtained from the inverse Fourier transform of the wavevector-frequency spectrum. Various models of wavevector-frequency spectrum have been investigated and compared with experimental data. Recent publications by Chase (1991, 1993) and Dowling (1998) demonstrate the near wall viscous shear stress contributions to the low wavenumber pressures should be included. Judging from the consistency with theories and data, Chase's 1987 inviscid flow spectrum is the most theoretically rigorous model. By combining this model with Chase's 1993 semi-empirical shear stress model, a so called "Combined Chase Spectrum" is developed and presented as the most comprehensive model for underwater applications. A point frequency spectra assessment suggested the most recently published models by Smol'yakov (2000) and Goody (2002) are the most accurate.

A verification analysis indicated there is little distinction between using the Modified Corcos spectrum and the Combined Chase spectrum for pressure sensor sizes up to one inch and frequencies as high as 20 kHz. The reasons for this are: (1) At low and mid frequencies, the excitation is dominated by the convective ridge and the subconvective region (the higher wavenumber portion of the low wavenumber region), where there is little difference between the two spectra. The differences occur at lower wavenumbers (including the acoustic region) which are not the dominant source at low and mid frequencies, (2) At higher frequencies, the Combined Chase non acoustic low wavenumber spectra are close to that of the Modified Corcos spectra (see Fig. 14), and (3) In the frequency range reported, the acoustic region has no dominant influence in the excitation due to the limitation of the sensor area. The differences may only be realizable when predictions are made for a large array of sensors or a large structure. Using Smol'yakov's (2000) point frequency model in conjunction with the normalized Modified Corcos wavevector-frequency spectrum (normalized by $\phi_p(\omega)(U_c/\omega)^2$), pressure spectra are predicted with reasonable accuracy up to 20 kHz measured by hydrophones from 0.1-inch to 1-inch diameter flush mounted on various buoyancy propelled vehicles. This prediction involves the whole range of wavenumbers since in a larger hydrophone, such as the 1-inch phone at 42 knots, the excitations are dominated by the low-wavenumber wall pressures above 5 kHz. For analysis using finite-element structural models, the Modified Corcos cross-spectral density function is recommended due to its simplicity and applicability to a broad range of wavenumbers and frequencies. Nonetheless, both the wavevector-frequency spectral and cross-spectral density models will be continuously updated and improved as new data becomes available.

The spectral models presented in this report are applicable to low-speed equilibrium flows, and are mostly semi-empirical models evolved from the physical understandings acquired from the classical analyses in fluid dynamics and acoustics. Computational fluid dynamics is an emerging field for the calculation of turbulent flows. Direct numerical simulation (DNS; e.g., Hansen, Handler, Leighton, and Orszag, 1987; Choi and Moin, 1990), large eddy simulation (LES; e.g., Hughes, Mazzei, and Oberai, 2001), or a hybrid of RANS (Reynolds-Averaged Navier-Strokes) and LES modeling technique (e.g., Peltier, Zajaczkowski, and Wyngaard, 2000) have been used with success, particularly at low Reynolds numbers. A thorough review on the progress and accomplishment in this field may help to gain further understanding to resolve some of the modeling issues on TBL wall pressures. In non-equilibrium flows, the effects of pressure gradients (e.g., Schloemer, 1967, Cipolla and Keith, 2000) and the laminar-turbulent transitions (e.g., Josserand and Lauchle, 1990; Marboe, 2000; Snarski, 2000) are important. These effects are not well understood, and are not covered in this study. A similar analysis shown in this report may prove to be fruitful to provide a useful modeling guideline to predict these effects.

REFERENCES:

1. Abarbanel, H. D., Katz, R. A., and Cembrola, T. W. (1994). "Nonlinear Analysis of High-Reynolds-Number Flows Over Buoyant Axisymmetric Body," Physical Review E, **49**(5), 4006-4018.

2. Abraham, B. M., and Keith, W. L. (1998). "Direct measurements of turbulent boundary layer wall pressure wavenumber-frequency spectra," Journal of Fluid Engineering, **120**, 29-39,

3. Bakewell, H. P. (1968). "Turbulent wall-pressure fluctuations on a body of revolution," J. Acoust. Soc. Amer. **43**, 1358-1363.

4. Blake, W. K. (1986). *Mechanics of Flow-Induced Sound and Vibration, Vol. I & II* (Academic Press, New York).

5. Bull, M. K. (1996). "Wall pressure fluctuations beneath turbulent boundary layers: Some reflections on forty years of research," J. Sound Vib. **190**(3), 299-315.

6. Capone, D. E., and Lauchle, G. C. (1995). "Calculation of turbulent boundary layer wall pressure spectra," J. Acoust. Soc. Amer. **98** (4), 2226-2234.

7. Chase, D. M. (1980). "Modeling the wavevector-frequency spectrum of turbulent boundary layer wall pressure," J. Sound and Vib. **70**, 29-67.

8. Chase, D. M. (1987). "The character of turbulent wall pressure spectrum at subconvective wavenumbers and a suggested comprehensive model," J. Sound Vib. **112**(1), 127-147.

9. Chase, D. M. (1991). "Fluctuations in wall-shear stress and pressure at low streamwise wavenumbers in turbulent -boundary-layer flow," J. Fluid Mech. **225**, 545-555.

10. Chase, D. M. (1993). "A semi-empirical model for the wavevector-frequency spectrum of turbulent wall-shear stress," J. Fluids and Structures **7**, 639-659.

11. Choi, H., and Moin, P. (1990). "On the space-time characteristics of wall pressure fluctuations," Phys. Fluids A. **2**(8), 1450-1460.

12. Cipolla, K., and Keith, W. (2000). "Effects of pressure gradients on turbulent boundary layer wavenumber frequency spectra," AIAA Journal, **38**(10), 1832-1836.

13. Cockburn, J. A., and Robertson, J. E. (1974). "Vibration response of spacecraft shrouds to in-flight fluctuating pressures," J. Sound Vib. **33**(4), 399-425.

14. Corcos, G. M. (1962). "Pressure fluctuations in shear flows," University of California, Institute of Engineering Research Report Series **183**, No. 2.

15. Corcos, G. M. (1963). "Resolution of Pressure in Turbulence," J. Acoust. Soc. Amer. **35**(2), 192-199.

16. Corcos, G. M. (1964). "The structure of the turbulent pressure field in boundary-layer flows," J. Fluid Mech.**18**, 353-378.

17. Corcos, G. M. (1967). "the resolution of turbulent pressures at the wall of a boundary layer," J. Sound Vib. **6**(1), 59-70.

18. Curle, N. (1955). "The influence of solid boundaries upon aerodynamic sound," Proc. Roy. Lond., **A231**, 505-514.

19. Davies, H.G. (1971). "Sound from turbulent-boundary-layer-excited panels," J. Acoust. Soc. Amer. **49**(3, part 2), 878-889.

20. Dowling, A. P., Ffowcs Williams, J. E. (1983). *Sound and Sources of Sound* (Halsted Press, a division of John Wiley & Sons, New York).

21. Dowling, A.P. (1992). "Flow Noise on Surfaces," *Modern Methods in Analytical Acoustics* (Lecture Notes, with Crighton, D.G., Ffowcs Williams, J.E., Heckl, M., and Leppington , pp.453-509, F.G., Springer-Verlag, London).

22. Dowling, A. P. (1998). "Underwater Flow Noise," Theorect. Comput. Fluid Dynamics, **10**, 135-153.

23. Efimtsov, B. M. (1982). "Characteristics of the field of turbulent wall pressure fluctuations at large Reynolds numbers," Sov. Phys. Acoust. **28**(4), 289-292.

24. Elswick, R. C. (1983). "Personal communication."

25. Farabee, T. M., and Geib, F. E. (1976). "Measurements of boundary layer pressure fields with an array of pressure transducers in a subsonic flow," Naval Ship Research and Development Center Technical Report, NSRDC Report No. 76-0031.

26. Farabee, T. M. (1986). "An experimental investigation of wall pressure fluctuations beneath non-equilibrium turbulent flows," David Taylor Naval Ship Research and Development Center Technical Report, DTNSRDC-86/047.

27. Farabee, T. M., and Casarella, M. J. (1991) "Spectral features of wall pressure fluctuations beneath turbulent boundary layers," Phys. Fluids A. **3**, 2410-2420.

28. Favre, A., Gaviglio, J., and Dumas, R. (1957). "Space-time double correlations and spectra in a turbulent boundary layer," J. Fluid Mech. **2**, 313.

29. Fisher, M. J., and Davies, P. O. A. L. (1963). "Correlation measurements in a non-frozen pattern of turbulence," J. Fluid Mech., **18**, 97-116.

30. Ffowcs Williams, J. E. (1982). "Boundary-layer pressures and the Corcos model: a development to incorporate low-wavenumber constrains," J. Fluid Mech. **125**, 9-25.

31. Goody, M. C. (2002). "An Empirical Spectral Model of Surface-Pressure Fluctuations that Includes Reynolds Number Effects," AIAA paper, AIAA-2002-2565, 8th AIAA/CEAS Aeroacoustics Conference and Exhibit, Breckenridge, Colorado.

32. Gradshteyn, I. S., and Ryzhik. (1965). *Table of Integrals, Series, and Products* (Academic Press, New York and London).

33. Graham, W.R. (1997). "A comparison of models for the wavenumber-frequency spectrum of turbulent boundary layer pressures," J. Sound Vib. **206**(4), 541-565.

34. Haddle, G. P. and Skudrzyk, E. J. (1969). "Physics of flow noise," J. Acoust. Soc. Amer. **46**(1, part 2), 130-156.

35. Hambric, S. A. and Hwang, Y. F. (2000). "Vibrations of Flat Plates Excited by Highly Subsonic Turbulent Boundary Layers," in Proceedings of Inter-Noise, Nice, France, pp. 27-30.

36. Han, F., Bernhard, R J., and Mongeau, L. G. (1999). "Prediction of flow-induced structural vibration and sound radiation using energy flow analysis," J. Sound Vib. **227**(4), 685-709.

37. Hansen, R. J., Handler, R. A., Leighton, R. I., and Orszag, S. A., "Prediction of Turbulence-Induced Forces on Structures from Full Numerical Solutions of the Navier-Strokes Equations," Jour. Fluids Structures, 1, 431-443, (1987).

38. Howe, M. S. (1992). "A note on the Kraichnan-Phillips theorem," J. Fluid Mech. **234**, 443-448.

39. Howe, M. S. (1998). *Acoustics of Fluid-Structure Interactions* (Cambridge University Press).

40. Hughes, T. J. R., Mazzei, L., Oberai, A. A., Wray, A. A. (2001). "The Multiscale formulation of large eddy simulation: decay of homogeneous isotropic turbulence," Phys. Fluids, **13**(2), 505-512.

41. Hwang, Y.F. (1998). "A Discrete Model of Turbulence Loading Function for Computation of Flow-Induced Vibration and Noise," in Proceedings of 1998 IMECE, Noise Control and Acoustics Division, pp. 389-395.

42. Josserand, M.A., and Lauchle, G.C. (1990). "Modeling the Wavevector-Frequency Spectrum of Boundary-Layer Wall Pressure During Transition on a Flat Plate," Trans. ASME – J. Vib. Acoust. **112**, 523-534.

43. Keith, W. L., Hurdis, D. A., and Abraham, B. M. (1992). "A comparison of turbulent boundary layer wall pressure spectra," J. Fluid Eng. **114**(3), 338-347.

44. Keith, W. L., and Abraham, B. M. (1997). "Effects of convection and decay of turbulence on the wall pressure wavenumber-frequency spectrum," J. Fluid Eng. **119**, 50-55.

45. Ko, S. H. (1991). "Analytical evaluation of a flush-mounted hydrophone array response to a modified Corcos turbulent wall pressure spectrum," Naval Undersea System Center Technical Report, TR 8943.

46. Ko, S. H., and Schloemer, H. H. (1992)."Flow noise reduction techniques for a planar array of hydrophones," J. Acoust. Soc. Amer. **92**(6), 3409-3424.

47. Kraichnan, R. H. (1956). "pressure fluctuations in turbulent flow over a flat plate," J. Acoust. Soc. Amer. **28**(3), 378-390.

48. Kronauer, R. E., Hollis, P.G., Bullock, K. J., and Lai, J. C. S. (1997). "How to estimate the low wavenumber turbulence frequency spectrum," Experiments in Fluids **23**, 353-360.

49. Lauchle, G. C., and Park, S. (2000). "Low-wavenumber wall pressure fluctuations due to boundary-layer transition," Applied Research Laboratory, Pennsylvania State University, Technical Memorandum No. 00-100.

50. Martin, N. C., and Leehey, P. (1977). "Low wavenumber wall pressure measurements using a rectangular membrane as a spatial filter," J. Sound Vib. **52**, 95-120.

51. Martin, N. C. (1976). "Wavenumber filtering by mechanical structures." Ph. D. Thesis, MIT, Cambridge, Massachusetts.

52. Marboe, R. C. (2000). "Acoustic emissions from unsteady transitional boundary layer structures," Pennsylvania State University, Applied Research Laboratory Technical Report No. TR 00-002.

53. Morrison, W. R. B., Bullock, K. J., and Kromauer, K. (1971). "Experimental evidence of waves in the sublayer," J. Fluid Mech. **47**, 639-656.

54. Morse, P. M., and Ingard, K. U. (1968). *Theoretical Acoustics* (McGraw Hill, New York).

55. Peltier, L. J., Zajaczkowski, F.J., and Wyngaard, J. C. (2000). "A Hybrid RANS/LES approach to large-eddy simulation of high-Reynolds-number wall-bounded turbulence," in Proceedings of ASME FEDSM'00: ASME 2000 Fluids Eng. Div. Summer meeting, Boston, Massachusetts.

56. Powell, A. (1958). "On the Response of Structures to Random Pressures and to Jet Noise in Particular," in *Random Vibration* (edited by Crandall, S. H., John Wiley and Sons, New York).

57. Phillips, O. M. (1956). "On the Aerodynamic Surface Sound from a Plane Turbulent Boundary Layer," Proc. Roy. Lond. **234**, 327-335.

58. Sevik, M. M. (1986). "Topics in hydroacoustics," in Proceedings of IUTAM Symposium Aero- and Hydroacoustics, Lyon (Springer-Verlag, Berlin).

59. Sherman, C. H., Ko, S. H., and Buehler, B. G. (1990). “Measurement of the turbulent boundary layer wave-vector spectrum,” J. Acoust. Soc. Amer. **88**(1), 386-390.

60. Smolyakov, A. V., and Tkachenko, V. M. (1991). “Model of a Field of Pseudosonic Turbulent Wall Pressures and Experimental Data,” Sov. Phys. Acoust. **37**(6), 627-631.

61. Smolyakov, A. V. (2000). “Calculation of the Spectra of Pseudosound Wall Pressure Fluctuations in Turbulent Boundary Layers,” Acoustical Physics **46**(3), 342-347 (translated from Akusticheskii Zhurnal, **46**(3), 410-407, 2000).

62. Snarski, S. R. (2002). “Measurement and modeling of the fluctuating wall pressure field beneath transitional boundary layer,” in Proceedings of ASME FEDSM’02: ASME 2002 Fluids Eng. Div. Summer meeting, Montreal, Canada.

63. Willmarth, W. W. (1975). “Pressure fluctuations beneath turbulent boundary layers,” in *Annual Review of Fluid Mechanics*, **7**, 13-37.

64. Willmarth, W. W. (1958). “Space-time correlations of the fluctuating wall pressure in a turbulent boundary layer,” J. Aerosp. Sci. **25**, 335-336.

65. Willmarth, W. W., and Wooldridge, C. E. (1962). “Measurements of the fluctuating wall pressure at the wall beneath a thick turbulent boundary layer,” J. Fluid Mech. **14**, 187-210.

66. Willmarth, W. W., and Roos, F. W. (1965). “Resolution and structure of the wall pressure field beneath a turbulent boundary layer,” J. Fluid Mech. **22** (1), 81-94.

67. Witting, J. M. (1986). "A Spectral Model of Pressure Fluctuations at a Rigid Wall Bounding an Incompressible Fluid, Based on Turbulent Structures in the Boundary Layer," Noise Control Engineering Journal **26**(1), 28-43.